Novel Nonporous Fouling-Resistant Composite Nanofiltration Membrane and Membrane Separation Systems for Wastewater Treatment Important for CPSON5/PPSON1: Minimization of Oily and Non-Oily Wastewater

Final Report
Contract Number CP/1108
Contract Period: June 4, 1998 to June 4, 2001

submitted to

Strategic Environmental Research and Development Program

by

Professor Benny D. Freeman
NC State University
Department of Chemical Engineering
Raleigh, NC 27695-7905

September, 2001

EXECUTIVE SUMMARY

Navy ships generate large volumes of wastewater (about 20-70 gal/day of water per crew member) which, to meet new regulations, require treatment prior to overboard discharge. In the past, all wastewater was simply discharged overboard. More recently, regulating bodies such as MARPOL, the EPA, the U.S. Coast Guard, and some states have enacted restrictions on the location and extent of such discharges.

Polymeric nanofiltration/ultrafiltration membranes able to produce dischargeable water have already been considered for shipboard wastewater treatment. The problem with this approach is fouling of the membrane by a layer of colloidal and particulate material that forms a secondary barrier to flow through the membrane. To overcome the problems of membrane fouling and the need for periodic cleaning, NC State University (NCSU) and Membrane Technology and Research, Inc. (MTR) have developed a new type of composite membrane in which a thin, highly water-permeable polymer coating layer is used to completely eliminate internal membrane fouling and significantly reduce the effect of surface fouling.

In this three-year research project, the focus of the first year was selection and optimization of the membrane materials. In the second year, membranes were prepared with industrial-scale equipment, a module test system was built, and the first bench-scale membrane modules were made. In the third year, the optimum membrane and module configuration was selected and several long-term runs were performed with solutions chosen to model shipboard wastewater. Composite nanofiltration membranes prepared with laboratory- and industrial-scale membrane manufacturing equipment had water fluxes in the range 150 to 200 $L/m^2 \cdot h$ at 150 psig. Their molecular weight cutoff was between 5,000 and 10,000 dalton. Bench-scale membrane modules were very resistant to fouling with oil/water emulsions containing up to 5% oil in tests lasting up to 80 days and in tests with graywater surrogate mixtures. Stable fluxes of 50 $L/m^2 \cdot h$ were obtained with oil emulsions and 20-40 $L/m^2 \cdot h$ with graywater surrogate mixtures. The permeate from these membranes would meet the new discharge regulation set by the MARPOL agreement.

The membrane modules can be cleaned satisfactorily by a clean water rinse cycle and even better by a cleaning technique developed during the project. The technique seems particularly suitable for shipboard oily and non-oily wastewater treatment systems. The technology is now ready for evaluation at the pilot-scale using a 1,000- to 5,000-gal/day unit operating pier-side to treat Navy ship wastewaters.

Table of Contents

List of Figures

List of Tables

1. PROJECT BACKGROUND, OBJECTIVE, AND TECHNICAL APPROACH

Navy ships generate large volumes of wastewater (about 20-70 gal/day of water per crew member) which, to meet new regulations, require treatment prior to overboard discharge. The wastewater is generally segregated into three streams according to the source. Blackwater is the sanitary water from commodes, urinals, and garbage grinders. Graywater includes galley water from sinks and kettles; turbid water from showers and laundry; and drainage water from air conditioners, drinking fountains, and interior deck drains. An additional wastewater is the secondary oily wastewater from parallel-plate separation of oil/water mixtures that accumulate in the bilge of a ship.

In the past, all wastewater was simply discharged overboard. More recently, regulating bodies such as MARPOL, the EPA, the U.S. Coast Guard, and some states have enacted restrictions on the location and extent of such discharges. These restrictions and the logistics of holding onboard and transferring to shore barges large volumes of wastewater have generated considerable interest in developing onboard wastewater treatment technology, called Marine Sanitation Devices. All new Navy ships will be fitted with these devices to minimize the environmental impact of shipboard wastewater.

The Carderock Division, Naval Surface Warfare Center, and its subcontractors have been working on this problem for some time. So far the most promising approach has been to use membrane bioreactors of various designs, which combine biological treatment with membrane separation. The goal of this project, funded by the Strategic Environmental Research and Development Program (SERDP), was to develop non-fouling composite nanofiltration membranes. In some cases such membranes would replace membrane bioreactors; in other cases the membranes would be combined with membrane bioreactors to improve reactor performance.

Polymeric nanofiltration/ultrafiltration membranes able to produce dischargeable water have already been considered for shipboard wastewater treatment. The problem with this approach is fouling of the membrane by a layer of colloidal and particulate material that forms a secondary barrier to flow through the membrane as shown in Figure 1. Surface fouling can be removed by periodic cleaning, but internal fouling caused by deposition of solid material in the interior of the membrane is generally irreversible.

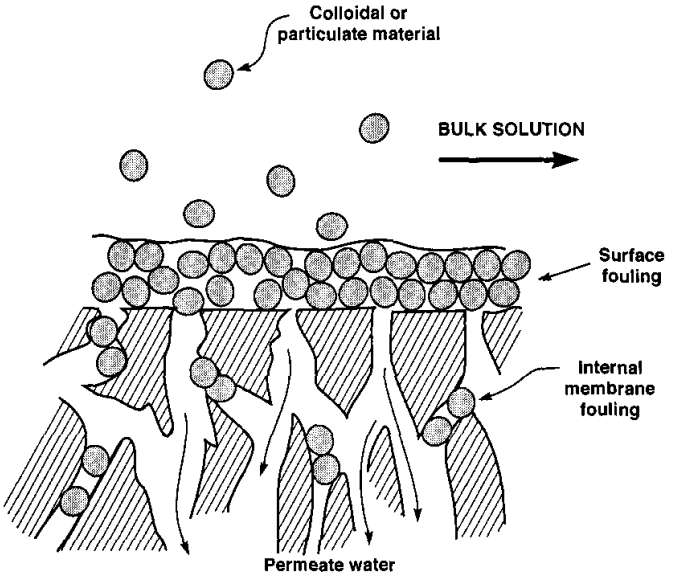

1 Schematic representation of fouling on an ultrafiltration membrane. *Surface fouling* is the deposition of solid material on the membrane that consolidates over time. Surface fouling is generally reversible. *Internal fouling* is caused by penetration of solid material into the membrane, which results in plugging of the pores. Internal membrane fouling is generally irreversible.

A typical plot illustrating the decrease in membrane flux that can result from membrane fouling is shown in Figure 2. The pure water flux of these membranes is approximately 50 gal/min but on contact with an aqueous emulsion, the flux immediately falls to about 10-12 gal/min. This first drop in flux is due to the formation of a gel layer on the membrane surface. Thereafter, the flux declines steadily over a two-week period. This second drop in flux is caused by densification of the gel layer under the pressure of the system. In this particular example the densified gel layer could be removed by periodic chemical cleaning of the membrane, which restored the flux to that of a new membrane. However, regular chemical cleaning as shown in Figure 2 is not suitable for a shipboard environment because of the quantity of chemicals and high maintenance involved.

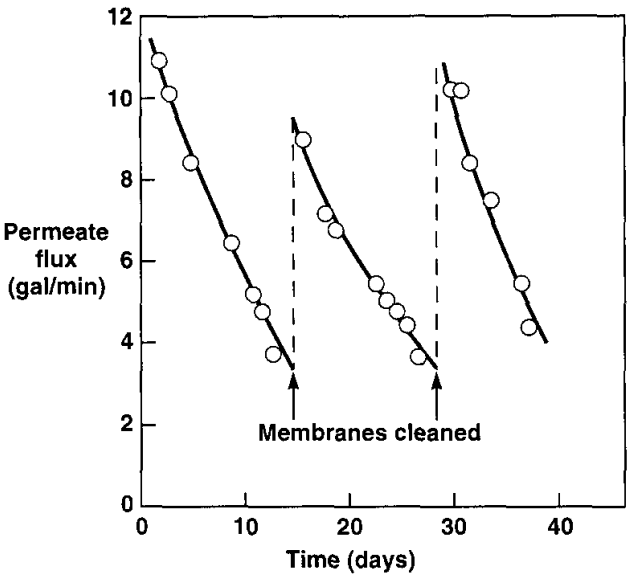

2 Ultrafiltration flux as a function of time for a latex emulsion. Because of fouling, the flux declines over a period of days. Periodic cleaning is required to maintain high fluxes.

If the regular cleaning cycle shown in Figure 2 is repeated many times, the membrane flux eventually does not return to the original value on cleaning. This slow, permanent lost of flux is due to internal fouling of the membrane by material that penetrates the membrane pores and becomes lodged in the interior of the membrane).

To overcome the problems of membrane fouling and the need for periodic cleaning, NC State University (NCSU) and Membrane Technology and Research, Inc. (MTR) developed a new type of composite membrane in which a thin, highly water-permeable polymer coating layer is used to completely eliminate internal membrane fouling and significantly reduce the effect of surface fouling. A microporous ultrafiltration support membrane is prepared first; this support is then coated with an extremely thin layer of a hydrophilic, water-swollen, but tough polymer. The configuration of this composite membrane is illustrated in Figure 3. We tried many coating materials during the course of this program, some available commercially and many synthesized and tested for the first time during this program. Results from these interim materials are well-documented in the progress reports submitted to SERDP during the course of this project. We obtained the best results with coating layers made from polyamide-polyether block copolymers (Pebax®, Elf Atochem, Philadelphia, PA), which have the basic structure shown in Figure 4. The polyamide blocks provide mechanical strength; the polyether blocks allow for high water permeability.

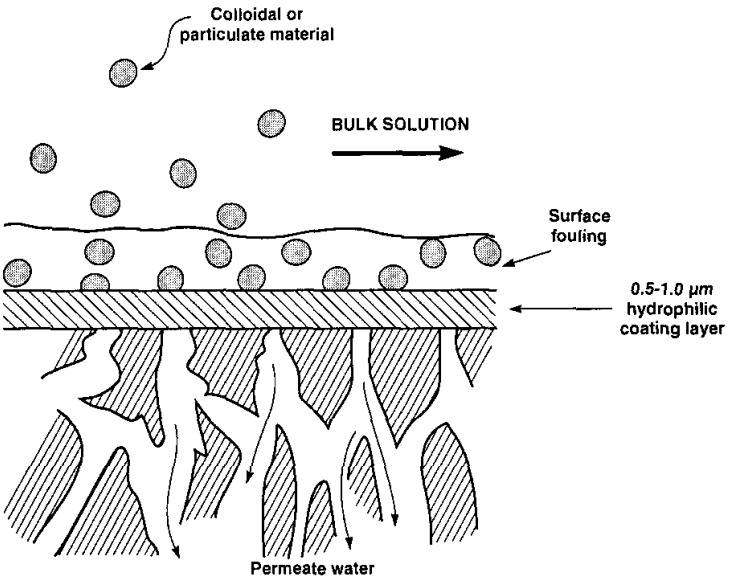

3 Schematic drawing of composite nanofiltration/ultrafiltration membrane in which a 0.5- to 1.0-micrometer-thick coating layer is used to eliminate internal membrane fouling and reduce the effect of surface fouling.

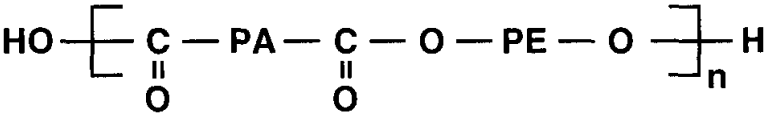

4 Repeat unit of polyamide (PA)-polyether (PE) block copolymers.

Coating the base ultrafiltration membrane with a thin polyamide-polyether layer produces a number of beneficial effects. First, internal membrane fouling is completely eliminated; colloids and particulates are retained by the coating layer and do not penetrate into the membrane pores. Therefore, the slow, irreversible decline in flux observed with conventional membranes does not occur. Second, the thin coating layer significantly enhances the rejection of the base membrane. For example, when tested with a 1% motor oil water emulsion our base membrane has an overall rejection of 90 to 95%, and the resulting permeate is still slightly cloudy. In contrast, the coated membrane has a rejection of more than 99%, and the permeate is completely clear. Also, the molecular weight cutoff of the uncoated membrane is about 50,000, whereas that of the coated membrane is about 5,000. Most importantly, the membrane flux is stable over long operating periods and can be regenerated to the original value without chemical treatment.

This was a three-year research project; the overall schedule for the project tasks is shown in Figure 5. The focus of the first year was selection and optimization of the membrane materials. In the second year, membranes were prepared with industrial-scale equipment, a module test system was built, and the first bench-scale membrane modules were made. In the third year, the optimum membrane and module configuration was selected and several long-term runs were performed with solutions chosen to model shipboard wastewater.

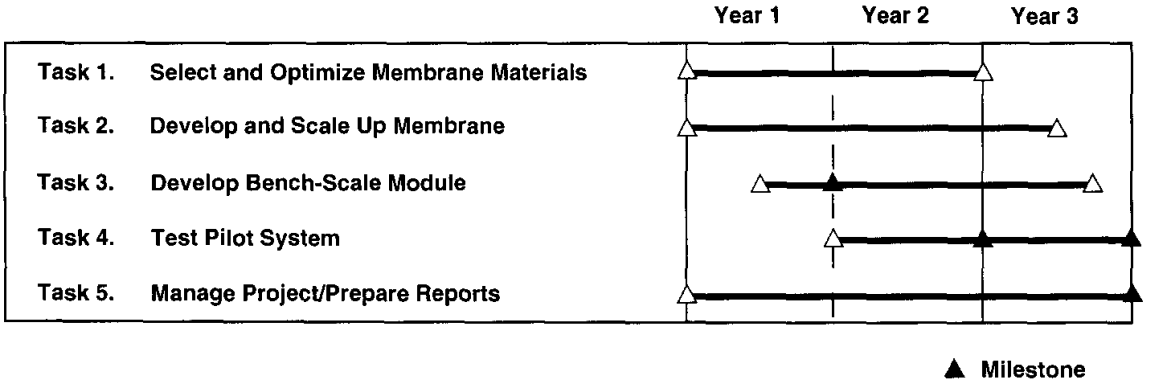

Figure 5. Project schedule.

2. RESULTS AND DISCUSSION

2.1 Membrane Preparation

The nanofiltration/ultrafiltration membranes used in this project consisted of a thin selective layer coated onto a microporous support membrane. Membrane production equipment at MTR was used for this two-step process.

The casting machine used to prepare the microporous support membrane is shown in Figure 6. The casting solution, consisting of a polymer dissolved in a water miscible-solvent, is doctored onto the moving web. The web passes into a water bath, which precipitates the polymer to form the film. The coated web is collected on a take-up roll, washed overnight to remove any remaining solvent and dried to form the support membrane.

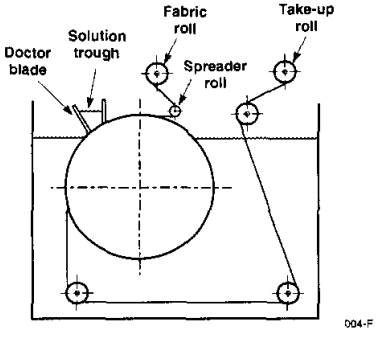

Figure 6. Schematic diagram of support membrane casting machine.

The apparatus used to apply the selective layer is shown in Figure 7. Support membrane from the feed roll passes into the coating tank, where a layer of polymer coating solution 50-100 micrometers thick is deposited. After solvent evaporation, a polymer film between 0.2 and 2.0 micrometers thick, depending on the polymer and the coating solution concentration, is left on the support membrane.

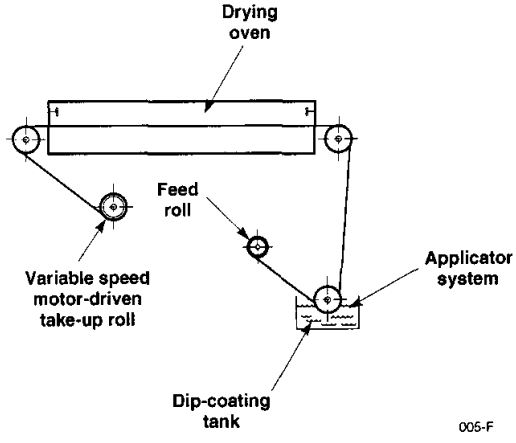

Figure 7. Schematic diagram of thin-film coating apparatus.

Three types of microporous support membrane were used during the project: poly(vinylidene fluoride) [PVDF], polysulfone [PSF], and polyetherimide [PEI]. In each case the microporous support was coated with a thin, nonporous layer of a Pebax polymer. Two hydrophilic grades, Pebax 4011 and 1074, were used for most of our work.

2.2 Composite Membrane Characterization

Gas permeation tests were used to determine the thickness of the Pebax layer and the integrity (absence of defects) of the membrane. Figure 8 shows a flow schematic of the pure gas test system.

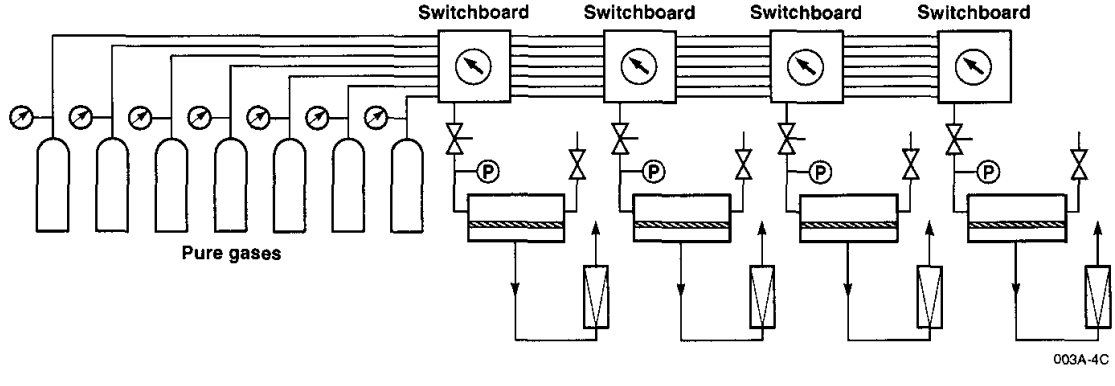

Figure 8. Schematic diagram of the test apparatus for measuring gas and vapor permeation through thin composite membranes. Because the membranes are thin, bubble flow meters can be used to measure the gas flow.

The rejection and flux characteristics of the membranes with solutions and emulsions were determined using the system shown in Figure 9. Up to six test cells can be connected in a series or parallel array to allow simultaneous side-by-side comparisons of several membrane stamps. Using this system, newly developed membranes were quickly screened to select the most promising for further study.

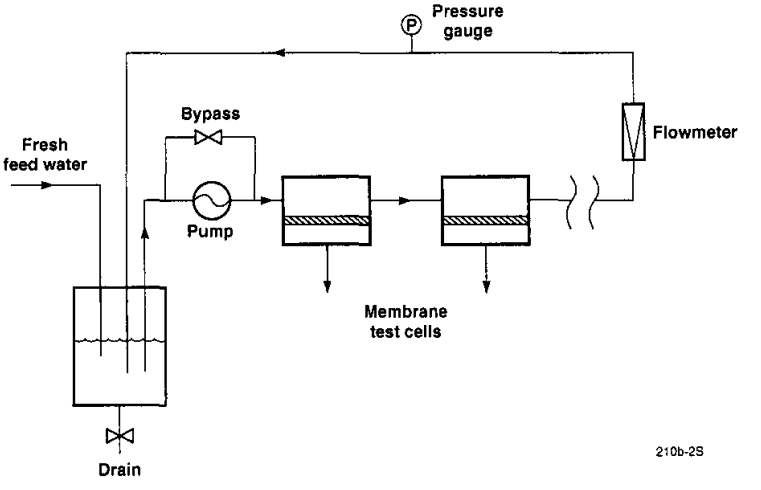

Figure 9. Simplified flow schematic of cross-flow test system with multiple test cells in series.

The flux and rejection were measured at each operational setting. The concentrations of the salt solutions were measured by conductivity, and the concentrations of the VOC solutions were measured by total organic carbon analysis (TOC) or gas chromatography.

2.3 Module Preparation

After completion of the membrane stamp tests, which demonstrated satisfactory performance of the Pebax 1074 and 4011 coated membrane, a series of rolls of 40-inch-wide membranes were prepared on industrial-scale equipment at MTR. This membrane was then used to fabricate bench-scale membrane modules. The winding operation used to prepare spiral membrane modules is shown schematically in Figure 10.

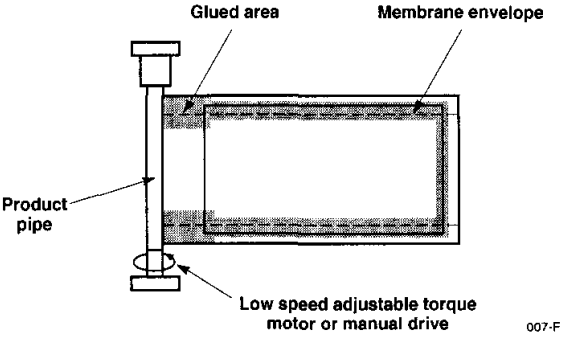

Figure 10. Schematic diagram of the module-winding operation.

The membrane is cut to size and folded around the feed-spacer material and the product distribution pipe. The membrane envelope is then moved to the wind-up machine. The product collection pipe is placed in the jaws of a motor clutch, and the spacer material is glued to the pipe. During the winding operation, the material is kept under slight tension, and the membrane envelope is glued along the edges and ends. When the operation is complete, a layer of reinforced tape is used to seal the module. The module is then fitted with end caps and placed in a pressure housing. A schematic diagram of a spiral-wound module is shown in Figure 11.

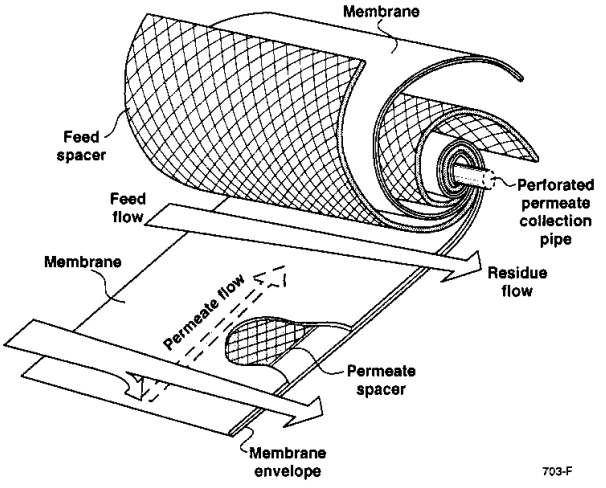

Figure 11. Schematic of spiral-wound module.

When preparing these membranes we had a number of problems with damage to the membranes by the feed spacer nettings. For example modules were prepared from Pebax membrane rolls that appeared to be defect-free and had carbon dioxide/nitrogen selectivities of 50 or more. However, the rolled modules had carbon dioxide/nitrogen selectivities of 3 to 5. The lower selectivity was due to a large increase in the nitrogen flux indicating membrane defects. Modules with low selectivities were dye tested by filling the feed side of the module with red dye solution and then drawing a vacuum on the permeate collection pipe. When the module is cut open, defects are apparent as small red marks. Dye test and visual inspection revealed very few membrane defects but it was difficult to obtain perfect modules. Some improvement was made by modifications to the module rolling procedure by placing less tension on the membrane, but perfect modules could not be made from this very thin composite membrane.

At this point a number of modules, shown to be apparently defective by the gas permeation tests, were tested with oil/water emulsions. The modules had oil emulsion rejections of greater than 99% and high fluxes; raffinose and PEG rejections were also comparable to the earlier membrane stamp data. Apparently, tiny membrane defects, which significantly affect the flux and selectivity of modules in tests with gases, have no measurable effect on modules in tests with aqueous emulsions and solutions. It is possible that swelling of the membrane by absorbed water closes defects present in the dry membrane.

2.4 Module Testing

Two module test systems were built for this program. A simplified flow diagram and a photograph of one of these units are shown in Figure 12. This system was originally built to operate with two 1 m^2 membrane modules but was later modified to operate with four modules. The system operates at feed pressure from 50 to 225 psig in a complete recirculation mode allowing continuous tests extending over several weeks to be performed. The permeate from each module can be collected and sampled separately so a continuous record of module performance can be obtained.

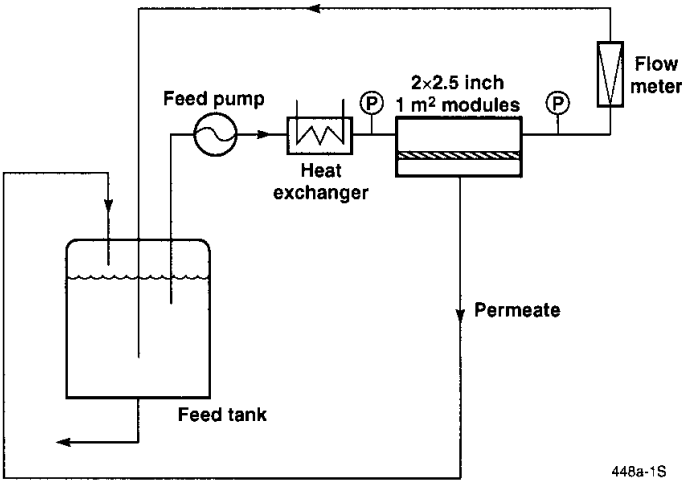

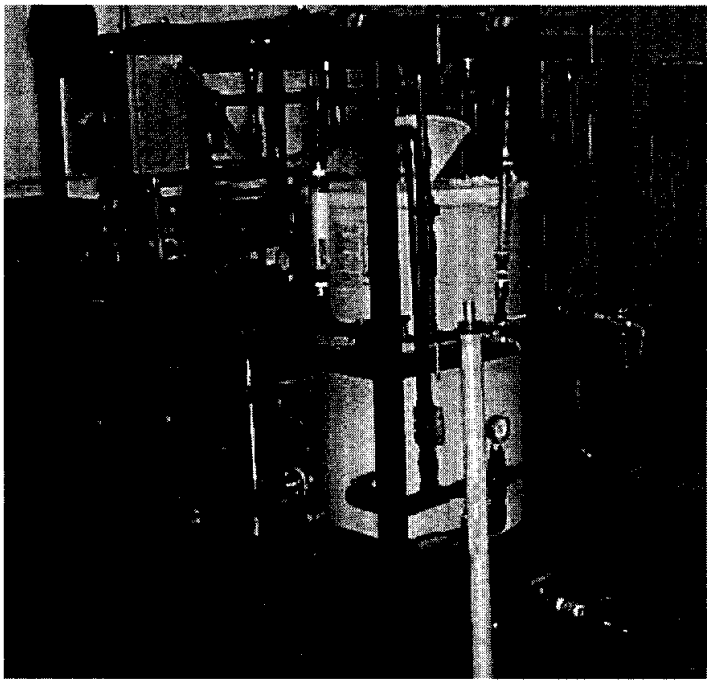

Figure 12. Flow schematic and photograph of one of the module test systems.

We found it much more difficult to completely wet membrane modules than membrane stamps. As a result, in some of our earlier tests, the module flux slowly increased during the first 10 days of operation as the membrane was gradually wetted and air was completely displaced from the PVDF support. To avoid this problem later modules were wetted before starting the tests by immersion in an ethanol solution and drawing a slight vacuum on the permeate side of the membrane. The module was then flushed with water to remove excess ethanol.

3. EXPERIMENTAL RESULTS AND DISCUSSION

3.1 Membrane Tests

Membranes were first tested by gas permeation to determine the thickness of the selective layer and its integrity (lack of defects). The water fluxes of defect-free membranes were determined and the membranes were also evaluated for chemical stability.

3.1.1 Membrane Characterization

The thickness of the selective Pebax layer was obtained in gas permeation tests by comparing the nitrogen flux of the composite membrane with the value for a thick isotropic film of the polymer. The absence of membrane defects was determined by comparing the nitrogen/carbon dioxide permeability ratio with the thick-film value. The thickness and number of defects in a membrane depend on the concentration and viscosity of the polymer coating solution, the method of applying the coating solution, and the properties of the support membrane. Defect-free layers as thin as 0.5 micrometers can be made. Some typical gas permeation test results obtained with the various support membranes and Pebax composite membranes are shown in Table 1.

Table 1. Gas Permeation Properties of Microporous Support Membranes [polysulfone, polyetherimide, and poly(vinylidene fluoride)] and Pebax 4011 and 1074 Thin-Film Composite Membranes.

Membrane Type	Pressure-Normalized Flux (10^{-6} cm^3(STP)/cm^2·s·cmHg)		Selectivity	Apparent Thickness of Pebax Layer (microns)
	N_2	CO_2	CO_2/N_2	
Polysulfone [PSF]	15,000	14,000	0.9	—
1? % Pebax 4011/PSF	0.47	22	47	1.7
2? % Pebax 1074/PSF	0.8	47	56	1.0
Polyetherimide [PEI]	38,300	35,200	0.9	—
1? % Pebax 4011/PEI	0.93	50	54	0.9
Poly(vinylidene fluoride) [PVDF]	188,000	199,000	1.1	—
2? % Pebax 4011/PVDF	1.7	83	49	0.5
2? % Pebax 1074/PVDF	1.1	57	53	0.7

The Pebax 4011 and 1074 composite membranes were all essentially defect-free as indicated by a carbon dioxide/nitrogen selectivity of more than 40 for each one. The apparent thickness of the Pebax layer ranged from 0.5 to 1.7 micrometers for the various membranes. The gas permeation results also showed that the Pebax-coated PVDF membrane had higher pure gas fluxes and thinner Pebax layers than equivalent membranes prepared on polysulfone or polyetherimide. Water permeability tests confirmed this result, so relatively early in the project we selected poly(vinylidene fluoride) [PVDF] as our standard microporous support material.

During the first two years of the project, our standard Pebax membrane had an initial pure water flux of about 40-60 L/m^2·h at 150 psig. Later we found that membranes with fluxes up to 200 L/m^2·h or more could be prepared by modifying the membrane preparation procedure. Initially membranes were made by coating a 0.5% Pebax solution onto the support membrane at 70°C and 1 ft/min. However, decreasing the temperature to 50°C and decreasing the coating speed to 0.3 ft/min produced membranes with three to five times higher fluxes and equivalent separation properties. The reason for this very large effect is not clear. The number of Pebax coatings applied to the membrane was also important, as illustrated by some typical results shown in Figure 13. The results also show that the flux of the Pebax 1074 membrane is about half that of a Pebax 4011 membrane made under the same conditions. However, the Pebax 1074 membrane is also more retentive, as shown by the data in Tables 2 and 3. For example, the Pebax 1074 membrane has about 70% rejection for raffinose (MW 595), indicating an approximate molecular weight cutoff of 1,000 to 2,000. The Pebax 4011 had 40% rejection for PEG (MW 1,500) indicating a molecular weight cutoff of 5,000 or more.

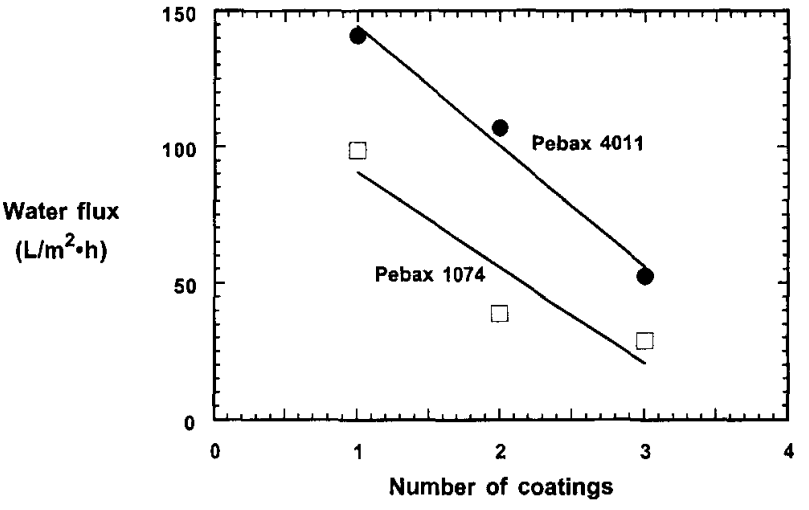

Figure 13. Water flux of Pebax composite membranes on a PVDF support as a function of the number of selective layer coatings with a 1% Pebax solution in butanol. The cross-flow permeation experiments were carried out at 100 psig pressure, 55 cm/s axial velocity, and 25°C. Feed solution was a model oily wastewater containing 900 ppm soybean oil and 100 ppm DC 193 surfactant.

Table 2. Solute Rejections of Pebax 1074/PVDF Composite Membrane. Feed pressure: 150 psig; feed flow rate: 0.34 gpm; feed temperature: 25°C; membrane area: 15.8 cm^2.

Solute	Solute Molecular Weight (g/mol)	Solute Rejection (%)
NaCl	58	10
$MgSO_4$	120	47
Sucrose	342	49
D-Raffinose	595	69
SDS	288	25
DDAPS	308	12
BDHAC	395	73
Brij®30	362	75
DC193	unknown	90

Table 3. Solute Rejections of 2% Pebax 4011/PVDF Composite Membrane. Feed pressure: 150 psig; feed flow rate: 0.34 gpm; feed temperature: 25°C; membrane area: 15.8 cm^2.

Solute	Solute Molecular Weight (g/mol)	Solute Rejection (%)
NaCl	58	3
$NaHCO_3$	84	14
$MgSO_4$	120	10
Na_3PO_4	164	24
PEG900	900	33
PEG1500	1,500	42

3.1.3 Membrane Chemical Stability Evaluation

The Pebax copolymers contain amide bonds in the nylon blocks, so potential degradation of the membrane by high or low pH solutions or by chlorine was a concern. Therefore, a series of tests were performed to determine the chemical stability of the membranes. The Pebax 1074/PVDF composite membranes were immersed in buffer solutions of pH 2, 3, 5, 8, 10 and 12 and in aqueous solutions of sodium hypochlorite (NaOCl) at concentrations of 10, 50, 100 and 1,000 ppm for one week. The NaOCl solutions were changed every two hours on the first day and then once each day thereafter. The stability of the membranes was determined by measuring the nitrogen and carbon dioxide fluxes before and after the test and the water flux at 150 psig. The pure gas fluxes and selectivities are shown in Table 4.

Table 4. Effect of pH and Sodium Hypochlorite Concentration on the Gas Permeation Properties of Pebax 1074/PVDF Composite Membrane Soaked for One Week in the Test Solution. Membrane area: 12.6 cm^2; feed pressure: 50 psig; feed temperature: 23 °C.

Soaking Solution	Pressure-Normalized Flux (10^{-6} cm^3(STP)/cm^2·s·cmHg)		Carbon Dioxide/Nitrogen Selectivity (-)
	Nitrogen	Carbon Dioxide	
Before Immersion	1.4	69	50
Buffer Solution pH			
2	4.1	116	29
3	3.5	102	30
5	1.5	59	40
8	2.7	125	46
10	4.7	138	30
12	Failed	—	—
NaOCl Concentration (ppm)			
10	3.2	133	42
50	3.5	123	36
100	3.4	131	38
1,000	Failed	—	—

The fluxes and selectivities of the membranes were essentially unaffected by exposure to solutions of pH between 3 and 10 or by exposure to NaOCl solutions containing up to 100 ppm NaOCl. Membranes exposed to very alkaline solutions of pH 12 or more and to a 1,000-ppm NaOCl solution both failed as shown by the very high fluxes and absence of selectivity in the gas permeation test. The membranes were then evaluated with aqueous solutions by measuring the water fluxes and rejections of a sodium chloride solution and of an oil/surfactant emulsion. The results are shown in Table 5.

Table 5. Water Fluxes and Solute Rejections of Pebax 1074/PVDF Composite Membranes After Being Soaked in Water, in Buffer Solutions of a Range of pHs, and in Sodium Hypochlorite Solutions for One Week. Membrane area: 15.8 cm^2; feed pressure: 150 psig; feed temperature: 23°C; feed flow rate: 0.34 gpm.

Soaking Solution	1,500 ppm NaCl		1,000 ppm oil/surfactant	
	Water Flux (L/m^2h)	Rejection (%)	Water Flux (L/m^2h)	Rejection* (%)
Untreated	35	13	32	92
Water	42	10	N/A	N/A
Buffer Solution pH				
2	62	12	46	92
3	42	12	36	92
5	29	13	27	90
8	33	12	30	90
10	60	15	60	91
12	65	16	56	90
NaOCl Concentration (ppm)				
10	31	11	38	92.3
50	25	11	32	92.5
100	45	10	N/A	N/A
1,000	24	15	N/A	N/A

* The oil emulsion used in this test contains 1,000 ppm oil and about 100 ppm surfactant. The membrane is slightly permeable to surfactant; therefore, a rejection of 90 to 95% corresponds to 100% rejection of the oil and 0 to 50% rejection of the surfactant.

The data in Table 5 show that the water fluxes and rejections of the membranes were essentially unaffected by exposure to the test solutions. From these experiments we conclude that the Pebax membrane is likely to be the chemically stable under normal operating conditions. However, exposure to very high pH solutions or very concentrated hypochlorite during chemical cleaning may be a problem.

3.2 Module Tests

3.2.1 Test Solutions

Modules were initially evaluated with water and then with various motor oil or vegetable oil emulsions using a neutral sufactant (DC193, Dow Corning, Midland, MI) as the stabilizing surfactant. These emulsions were quite stable and showed no sign of phase separation even in experiments lasting several weeks. The Carderock Naval Warfare Test Station has also devised a number of mixtures to model Navy ship waste. The composition of the test mixture that most closely matches graywater is shown in Table 6. Although the total solids concentration of the mixture is only

3,800 ppm, the solution has a very high membrane fouling potential. Membrane fluxes gradually fell two- to four-fold when exposed to this mixture.

Table 6. Model Wastewater Composition.

Component	Amount for 100 gallons (g)	ppm
Tide Powdered Laundry Detergent	33.0	87
Laundry Starch	151.5	400
Gelatin	56.8	150
NH_4Cl	190.0	500
NaCl	66.6	175
$Na_3PO_4 \cdot 12H_2O$	72.0	82
$NaHCO_3$	63.6	168
Canned Dog Food	757.6 (26.7 oz)	2,000
Crisco Solid Vegetable Shortening	26.5	70
Wesson oil	26.5	70
Directions		
Mix the components into the indicated amount of tap water. Heat to boiling for 30 minutes. Cool overnight and process the next day.		

3.2.2 Initial Flux and Rejection Tests

In a series of initial tests, the performance of Pebax 1074 modules was measured as a function of feed pressure, temperature and module flow rate with water as the test solution. The flux and rejection of various model solutions were also measured at the end of these tests under standard test conditions.

Figure 14 shows feed flow rate as a function of pressure drop across the module at various feed pressures. The feed-to-residue pressure drop of about 20 psig at a flow rate of 2 gpm was larger than expected. Therefore, we used a pressure drop of 10 psig as the base-case for module experiments; this is equivalent to a flow rate of about 1.1 gpm. Figures 15 and 16, respectively, show permeate water flux and pressure-normalized water flux as a function of average feed pressure. As expected, the water flux increases linearly with feed pressure and pressure-normalized water flux is independent of feed pressure. However, the water flux of the module was only 14 $L/m^2 \cdot h$ at 150 psig, half the expected value based on membrane cell tests. This occurred because the membrane was incompletely wetted.

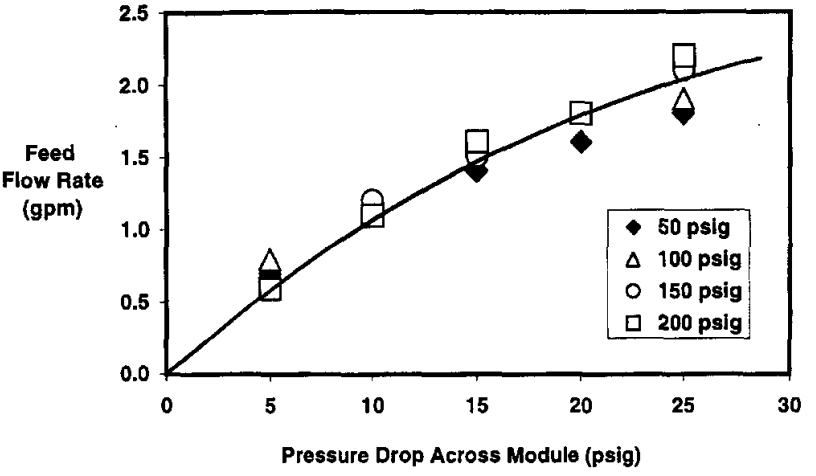

Figure 14. Feed flow rate of a Pebax 1074 module (#1510) as a function of pressure drop across the module. Feed solution: pure water; feed temperature: 21 °C; feed pressures: 50, 100, 150 and 200 psig; pressure drops across module: 5, 10, 15, 20 and 25 psig. Feed spacer: Nylon ROF030; permeate spacer: double Tricot 9944.

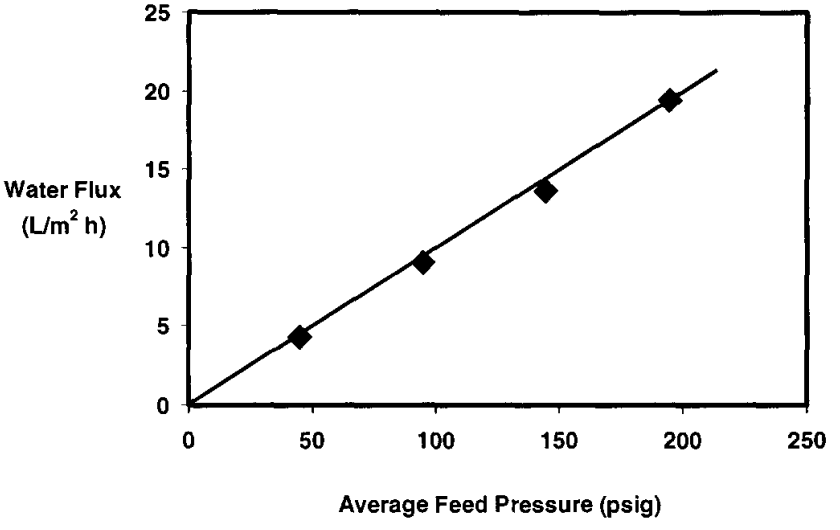

Figure 15. Water flux of a Pebax 1074 module (#1510) as a function of average feed pressure. Feed solution: pure water; feed temperature: 21 °C; feed pressures: 50, 100, 150 and 200 psig. Feed spacer: Nylon ROF030; permeate spacer: double Tricot 9944.

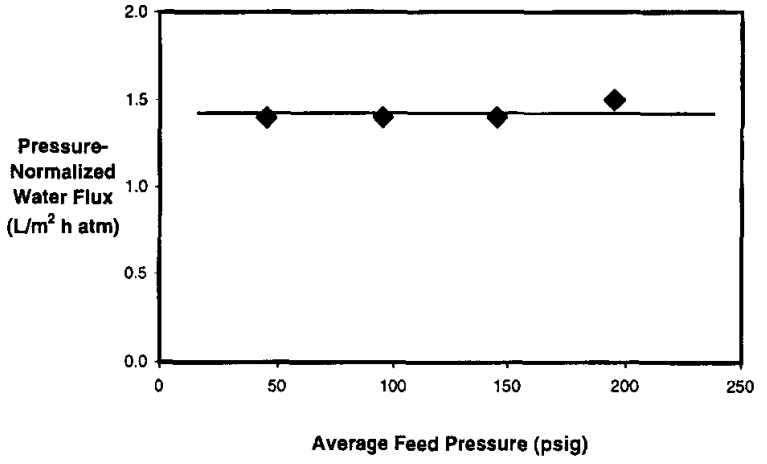

Figure 16. Pressure-normalized water flux of a Pebax 1074 module (#1510) as a function of average feed pressure. Feed solution: pure water; feed temperature: 21 °C; feed pressures: 50, 100, 150 and 200 psig. Feed spacer: Nylon ROF030; permeate spacer: double Tricot 9944.

The molecular weight cutoff of the Pebax 1074 module was then measured with a 1% motor oil emulsion and with polyethylene glycol, raffinose and toluene solutions. The tests were carried out at a feed pressure of 150 psig and a feed-to-residue pressure drop across the module of 10 psig. After tests with each solution, the system was flushed with water. The test data are given in Table 7. The membrane rejected essentially all of the motor oil emulsion. The permeate was completely clear and total organic carbon measurements showed less than 150 ppm organic carbon. The raffinose and PEG 3400 rejections were comparable to those measured earlier with membrane stamps. The molecular weight cutoff of the membrane is about 5,000.

Table 7. Water Fluxes and Solute Rejections of the Pebax 1074/PVDF Composite Membrane Module. Membrane area: 1 m^2; feed pressure: 150 psig; feed-to-residue pressure drop: 10 psig; feed temperature: 23 °C.

Aqueous Solution	Molecular Weight (g/mol)	Pebax 1074/PVDF Module (#1565)	
		Water Flux ($L/m^2 \cdot h$)	Rejection (%)
1% Motor Oil	N/A	43	99
1,000 ppm PEG	3,400	58	87
1,000 ppm Raffinose	595	62	41
250 ppm Toluene	92	55	11

3.2.3 Effect of Feed Spacers

The first modules tested were fabricated using the Nylon feed spacer and Tricot permeate spacer used in commercial pervaporation modules produced by MTR. However, because in this application the modules are likely to be operated with very dirty and highly fouling feeds, alternative, more open feed spacers were also evaluated. The properties of the candidate feed spacers tested are listed in Table 8.

Table 8. Candidate Feed Spacer Properties.

Spacer	Spacer Thickness (mil)	Configuration
ROF	25	90° Angle
ROF	30	0° Angle
ROF	30	90° Angle
MWN	48	—

Figure 17 shows the feed flow rate as a function of feed pressure for equivalent modules made with the three different spacers at a feed-to-residue pressure drop of 10 psi. The thicker MWN048 spacer has the highest flow rate and the ROF030 spacer the lowest. Based on these results, we selected the MWN048 spacer as our base-case feed spacer material.

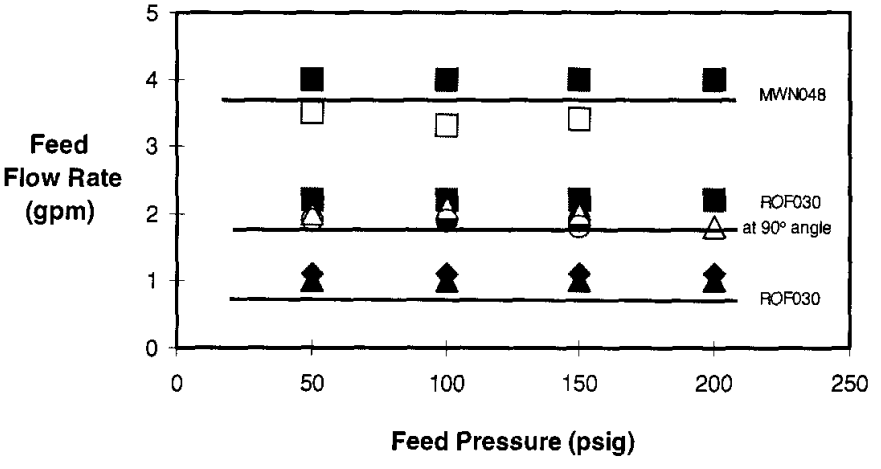

Figure 17. Feed flow rate as a function of average feed pressure for Pebax 1074 modules with various feed spacers

All modules were fitted with a single-layer Tricot 9944 permeate spacer; the membrane area was approximately 1 m^2. The modules were tested at 50 to 200 psig feed pressures and 5 to 20 psig feed-to-residue pressure drops across the modules. The modules were then operated with pure water; 1%, 2% and 3% motor oil emulsions; and finally with a 3,800-ppm graywater surrogate mixture over a

range of feed pressures. Figures 18(a) and (b) show the performance of Modules 1616 and 1617, respectively, which both had thin feed channel spacers. The results show clear evidence of concentration polarization and gel formation on the membrane surface. The oil-water emulsion fluxes increase with increasing pressure but then reach a limiting flux, after which any further increase in pressure does not increase the flux. Also, the limiting flux decreases with the fouling potential of the solution. For example, for Module 1616, the limiting flux with the 1% motor oil emulsion is 33 L/m^2·h, with the 2% motor oil emulsion 28 L/m^2·h, and with the 3% motor oil emulsion 20 L/m^2·h. The surrogate graywater is extremely fouling, with a limiting flux of only 10 L/m^2·h. In contrast, the data shown in Figure 18(c) for Module 1619, fitted with a 48-mil-thick feed spacer, was more encouraging. The module did not reach a limiting flux with motor oil emulsions, even at a flux of 50 L/m^2·h. However, with the highly fouling surrogate graywater solution, a limiting flux of 18 L/m^2·h was reached.

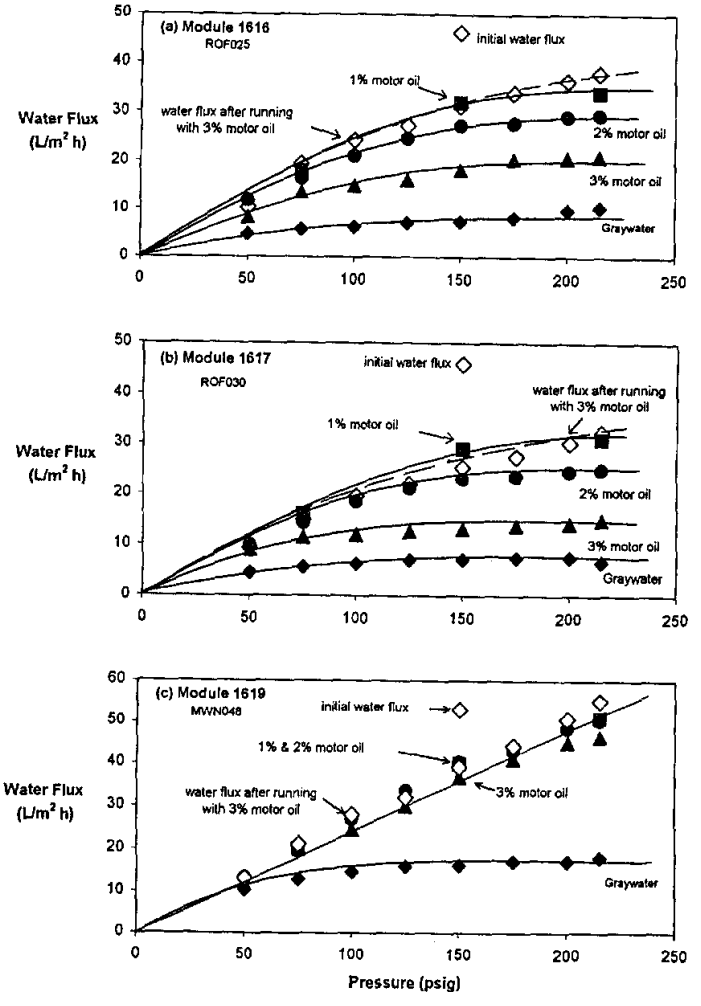

Figure 18. Water flux of Pebax 1074 modules having feed spacers (a) ROF025, (b) ROF030 and (c) MWN048 as a function of feed pressure. Temperature: 23 °C; pressures: 50 to 225 psig; feed-to-residue pressure drop across the module: 10 psig.

After the initial range-finding tests shown in Figures 16 and 17, the three test modules were operated at 150 psig feed pressure and a 10 psig feed-to-residue pressure drop across the modules for a further month. The data obtained are shown in Figure 19. First, the initial water fluxes of the modules were measured, then the water fluxes of the modules with 1%, 2% and 3% motor oil emulsions were measured. At the end of the eight-day motor oil emulsion tests, the system was flushed with water for three days and the water flux remeasured. Finally, the water fluxes of the modules were measured during operation with the graywater surrogate mixture for five days. After these tests, the modules were flushed with water and their fluxes measured again for comparison with their original values. Module 1619 with the thicker feed spacer, 48 mil, showed a significantly better performance than Modules 1616 and 1617, which had thinner feed spacers. It also appears that motor oil does not foul the Pebax membrane, but the graywater surrogate mixture does.

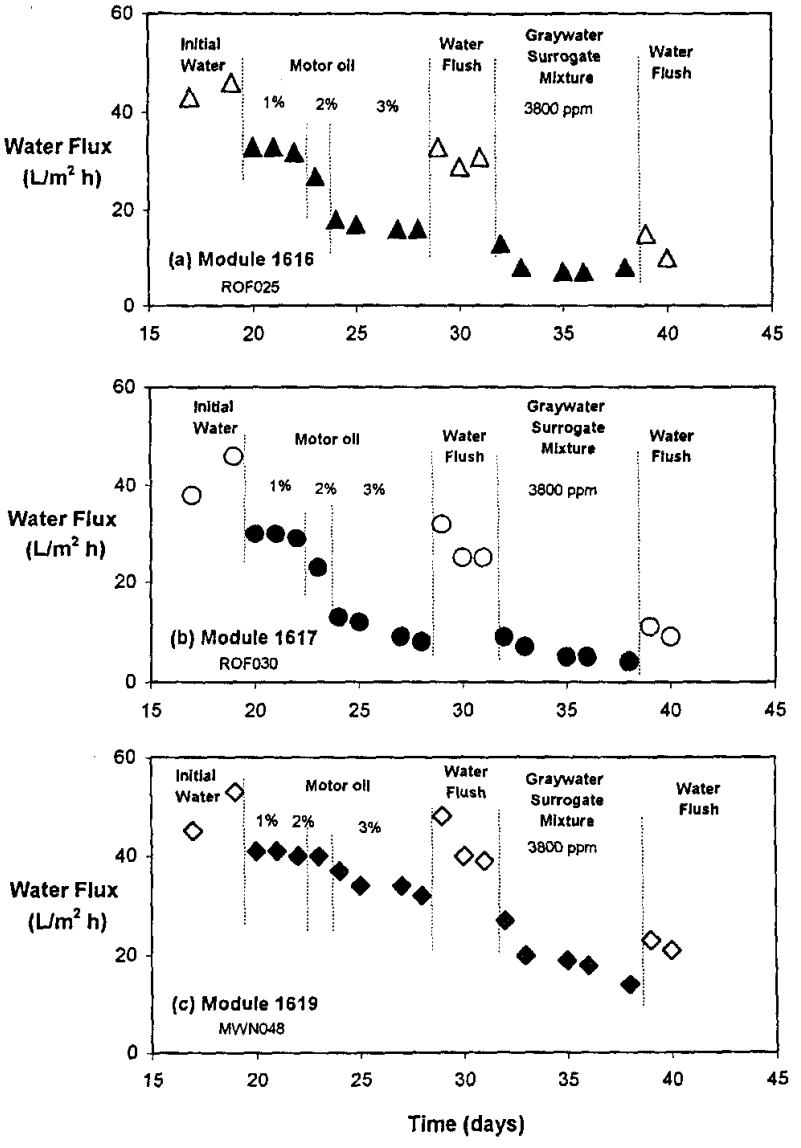

Figure 19. Water fluxes as a function of operating time for Pebax 1074/PVDF modules: (a) 1616 with an ROF025 spacer, (b) 1617 with an ROF030 spacer, and (c) 1619 with an MWN048 spacer. Temperature: 23 °C; pressure: 150 psig; feed-to-residue pressure drop across module: 10 psig.

3.2.4 Long-Term Tests

Several long-term tests to evaluate the performance of the Pebax spiral-wound modules with various feed solutions were performed. One such test to show the difference in performance of two equivalent bench-scale membrane modules, one using an uncoated PVDF ultrafiltration membrane and the other using the same membrane overcoated with a 0.5- to 1.0-micrometer thick Pebax 1074 layer is shown in Figure 20. Initially the uncoated PVDF membrane had a much higher flux than the coated membrane, but over a period of 22 days this flux declined 20-fold to approximately 12 $L/m^2 \cdot h$. In contrast, the initially lower coated membrane flux (50 $L/m^2 \cdot h$) was almost completely retained for the whole 22-day test. After the test period, both membranes were regenerated by flushing the system with clean water; no chemical additives or cleaning agents were used. The uncoated PVDF membrane only partially regained its original flux, showing that a large fraction of the flux decline was due to permanent internal membrane fouling. The flux of the coated membrane, however, returned to its original value. When both membranes were retested with the motor oil feed solution, the uncoated membrane flux quickly declined to a low value whereas the coated membrane maintained its previous high value.

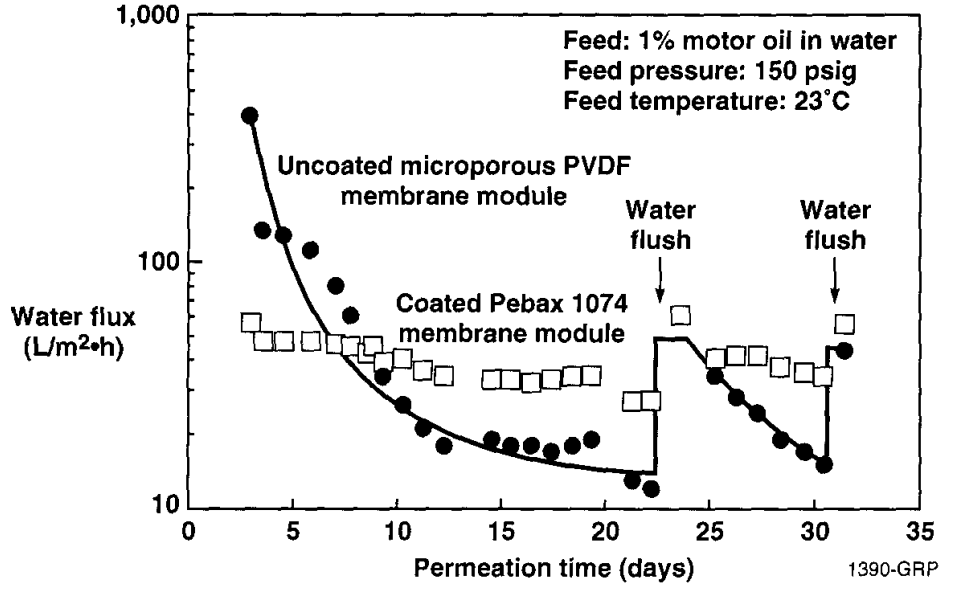

Figure 20. Change in flux over time for an uncoated microporous polyvinylidene fluoride (PVDF) ultrafiltration membrane module and the same membrane coated with a 0.5-1.0 micrometer polyether-polyamide layer (Pebax 1074). The PVDF module had a rejection of ~90%, the coated Pebax 1074 module had a rejection of more than 99%.

Similar results were obtained when currently available commercial ultrafiltration membranes were coated with Pebax. Figure 21 shows the performance of polysulfone tubular membranes produced by Zenon (Toronto, Canada) with and without a Pebax coating layer. The pure water flux of the uncoated Zenon membrane was 30 $L/m^2 \cdot h$, and that of the coated membrane was a little lower at 28 $L/m^2 \cdot h$. However, when tested with a 1,000-ppm oil/water emulsion the flux of the uncoated

membrane fell 10-fold to 2.5 L/m^2·h, whereas that of the coated membrane was essentially unchanged at 25 L/m^2·h.

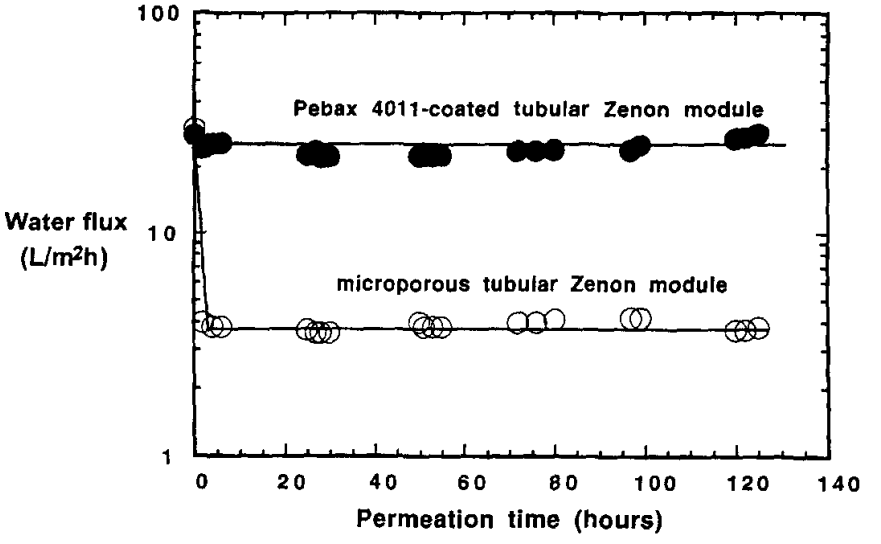

Figure 21. Water fluxes of uncoated and Pebax 4011-coated tubular Zenon membranes as a function of permeation time. Feed: 1,000 ppm soybean oil water emulsion; feed pressure: 20 psig; feed flow rate: 1.2 gpm; temperature: 25°C.

3.3 Module Cleaning

Several cleaning methods were evaluated for removal of the densified gel layer of retained materials from the membrane surface. The period of the cleaning cycle can vary from daily for food applications, such as ultrafiltration of whey, to once a month or more for ultrafiltration membranes used as polishing units in ultrapure water systems. A typical cleaning cycle is as follows:

1. Flush the system several times with hot water at the highest possible circulation rate.
2. Treat the system with an appropriate acid or alkali wash depending on the nature of the layer.
3. Treat the system with a hot detergent solution.
4. Flush the system thoroughly with water to remove all traces of detergent; measure the pure water flux through the membrane modules under standard test conditions.

Even after cleaning, some degree of permanent flux loss over time is expected. However, if the restoration of flux is less than expected, steps 1 through 3 are repeated.

However, the type of cleaning cycle shown above is not suitable for the low-maintenance requirements of Navy ships because of the need to use acidic or basic cleaning solutions. For most of our project we successfully cleaned membranes by circulating clean water through the modules

at high speed. Typical results are shown previously in Figure 20. Towards the end of this project a new module cleaning method called *in-situ* backflushing-flow reversal was developed. This procedure has considerable promise. A number of process developers have used methods such as flow pulsations and pressure variation to clean the membrane surface. The *in-situ* backflushing-flow reversal technique is illustrated in Figure 22.

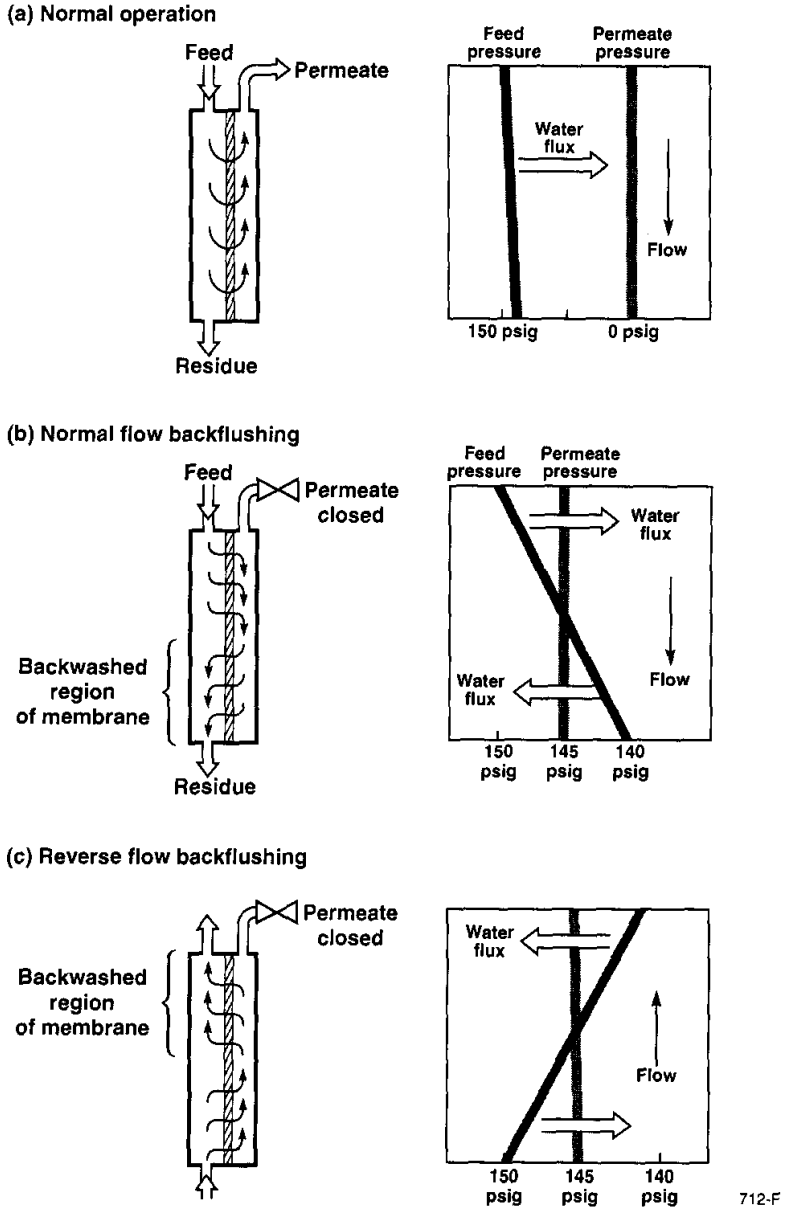

Figure 22. Backflushing, flow-reversal technique for cleaning membrane modules by closing the permeate port.

Figure 22(a) shows the membrane module in a normal operating mode. A pressure drop of about 10 psig exists across the membrane from the feed to the residue solution. This pressure difference is required to drive the feed solution through the module. The permeate pressure is close to atmospheric (0 psig). If the permeate port from the module is closed, the pressure on the permeate side of the membrane increases to a pressure intermediate between those of the feed and residue streams. This produces a slight positive pressure at one end of the module and a slight negative pressure at the other end of the module as shown in Figure 22(b). The back pressure difference sets up a backflushing condition in which permeate water that has permeated one-half of the module becomes a backflushing solution in the other half of the module. Deposited materials lifted from the membrane surface in the backflushed area are swept away by the fast feed flow. If the direction of the feed is reversed as shown in Figure 22(c), the other half of the module is then backflushed. This *in-situ* procedure allows a membrane module to be cleaned without stopping the normal operation of the membrane system. By using motor-driven valves, the entire procedure can be automated and set to clean the modules for a few minutes daily or even more frequently.

In the past this backflushing technique has been limited to low-pressure capillary ultrafiltration modules. Membranes in other modules are damaged by the reverse flow. However, the composite membranes we have developed are sufficiently tough to withstand this type of operation. Some preliminary results are shown in Figure 23. The starting point is a nanofiltration module used to concentrate an emulsion of 3.2 wt% motor oil. After 80 days of continuous operation, the membrane flux had fallen to 7 $L/m^2 \cdot h$. At this point the permeate valve was closed and the back half of the module was backflushed for one hour; the flux doubled to 15 $L/m^2 \cdot h$. After a further two days of normal operation the liquid flow was reversed, the permeate valve was again closed, and the second half of the module was backflushed for one hour. The membrane flux then rose to more than 30 $L/m^2 \cdot h$. Clearly the backflushing, flow-reversal procedure is a powerful method of *in-situ* membrane cleaning without using chemicals or halting normal operation of the process.

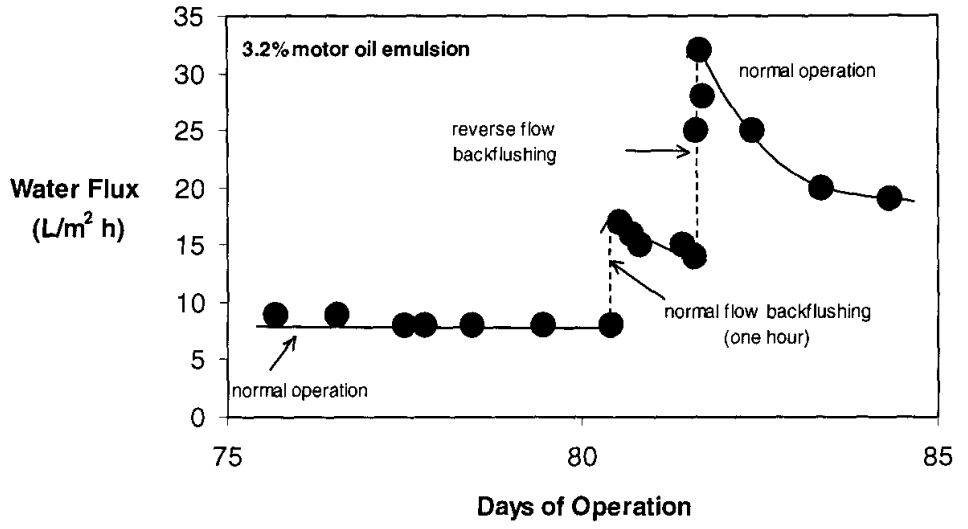

Figure 23. Backflushing, flow-reversal cleaning of a bench-scale nanofiltration Pebax 4011 composite membrane spiral-wound module. Feed solution was 3.2% motor oil at 150 psig.

4. CONCLUSIONS, TRANSITION PLAN AND RECOMMENDATIONS:

- Composite nanofiltration membranes prepared with laboratory- and industrial-scale membrane manufacturing equipment had water fluxes in the range 150 to 200 L/m^2·h at 150 psig. Their molecular weight cutoff was between 5,000 and 10,000 dalton.

- Bench-scale membrane modules were very resistant to fouling with oil/water emulsions containing up to 5% oil in tests lasting up to 80 days and in tests with graywater surrogate mixtures. Stable fluxes of 50 L/m^2·h were obtained with oil emulsions and 20-40 L/m^2·h with graywater surrogate mixtures. The permeate from these membranes would meet the new discharge regulation set by the MARPOL agreement.

- The membrane modules can be cleaned satisfactorily by a clean water rinse cycle and even better by an *in-situ* backflushing, flow-reversal technique. This technique seems particularly suitable for shipboard oily and non-oily wastewater treatment systems.

- The technology is now ready for evaluation at the pilot-scale using a 1,000- to 5,000-gal/day unit able to operate pier-side to treat Navy ship wastewaters.

We recommend that the Navy consider a larger scale application of these very promising membranes for pierside graywater testing and also consider the possible use of such membranes for oil/water separation. An ESTCP or other similar program would be a very useful next step in the development of this technology.

APPENDIX A: Publications and Patents

Two peer-reviewed publications (attached) related to coating materials development has already been published and is attached. Several patent applications are in preparation at MTR and they will be forwarded to SERDP as soon as possible.

ELSEVIER

Polymer 42 (2001) 9941–9948

polymer

www.elsevier.com/locate/polymer

Solubility and diffusivity of sodium chloride in phase-separated block copolymers of poly(2-dimethylaminoethyl methacrylate), poly(1,1′-dihydroperfluorooctyl methacrylate) and poly(1,1,2,2-tetrahydroperfluorooctyl acrylate)

Kazukiyo Nagai[a,b,1], Satoshi Tanaka[a], Yuichi Hirata[a], Tsutomu Nakagawa[a,*], Michelle E. Arnold[b], Benny D. Freeman[b,*], Denis Leroux[c,d,2], Douglas E. Betts[c,3], Joseph M. DeSimone[c], Francis A. DiGiano[d]

[a]*Department of Industrial Chemistry, Meiji University, Higashi-Mita, Tama-Ku, Kawasaki 214-0033, Japan*
[b]*Department of Chemical Engineering, North Carolina State University, Raleigh, NC 27695-7265, USA*
[c]*Department of Chemistry, University of North Carolina, Chapel Hill, NC 27599-3290, USA*
[d]*Department of Environmental Sciences and Engineering, University of North Carolina, Chapel Hill, NC 27599-7400, USA*

Received 27 February 2001; received in revised form 24 July 2001; accepted 26 July 2001

Abstract

Solubility and diffusivity of sodium chloride were determined in a series of dense films of phase-separated diblock and triblock copolymers composed of poly(2-dimethylaminoethyl methacrylate) (PDMAEMA) and either poly(1,1′-dihydroperfluorooctyl methacrylate (PFOMA) or poly(1,1,2,2-tetrahydroperfluorooctyl acrylate) (PTAN). As the content of hydrophilic PDMAEMA increases in PDMAEMA-*b*-PFOMA films, total water uptake increases. The salt partition coefficient of these films increases with increasing PDMAEMA content and weight fraction of water in the PDMAEMA domains. In contrast, salt diffusivity is not monotonically correlated with PDMAEMA content and effective hydration. Triblock copolymers exhibit different values of total water uptake, total hydration, salt partition, and diffusion coefficients than those of diblock copolymers (PDMAEMA-*b*-PFOMA) at the same PDMAEMA concentration. The total water uptake of PFOMA-*b*-PDMAEMA-*b*-PFOMA copolymers is lower than that of PDMAEMA-*b*-PFOMA, while water uptake of PTAN-*b*-PDMAEMA-*b*-PTAN films is higher than that of PDMAEMA-*b*-PFOMA. Salt partition and diffusion coefficients increase monotonically with the amount of freezing water in the hydrophilic domains, suggesting that the state of water in the phase-separated block copolymers is an important factor influencing their salt uptake and transport properties.

Keywords: Block copolymers; Freezing water; Salt transport

1. Introduction

The use of polymer membranes for drinking water and waste water treatment would be enhanced if lower-fouling membrane materials were available [1]. In one case, Hamza et al. [2] modified the surface of porous polyethersulfone ultrafiltration membranes with fluorotelomers and found that these modified membranes were less susceptible to fouling by oil/water mixtures than unmodified membranes. The modified membranes were more permeable than unmodified polyethersulfone ultrafiltration membranes to oil/water emulsions.

Fundamental transport properties of solutes such as sodium chloride (NaCl) were reported by Rosenbaum et al. for cellulose acetate [3] and by Yasuda et al. for various hydroxyalkyl methacrylate-based hydrogels [4,5]. On the basis of these studies, salt diffusivity decreases exponentially with decreasing reciprocal hydration, in qualitative agreement with the free volume theory of diffusion [3,4]. For highly hydrated samples, permeability coefficients also decrease exponentially with decreasing reciprocal hydration [4,5]. Salt partition coefficients are nearly equal to hydration

* Corresponding authors. Tel.: +81-44-934-7211; fax: +81-44-934-7906 (T. Nakagawa). Tel.: +1-919-515-2460; fax: +1-919-515-3435 (B.D. Freeman).

E-mail addresses: nakagawa@isc.meiji.ac.jp (T. Nakagawa), benny_freeman@ncsu.edu (B.D. Freeman).

[1] Present address: CSIRO Molecular Science, Private Bag 10, Clayton South, VIC., 3169, Australia.

[2] Present address: SiPix Imaging, Milpitas, CA 95035, USA.

[3] Present address: ONDEO-Nalco Chemical Company, Naperville, IL 60563-1198, USA.

0032-3861/01/$ - see front matter
PII: S0032-3861(01)00549-3

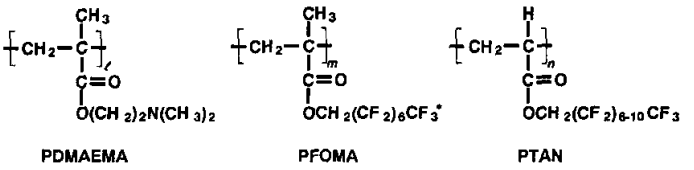

Fig. 1. Repeat units of poly(2-dimethylaminoethyl methacrylate) (PDMAEMA), poly(1,1′-dihydroperfluorooctyl methacrylate) (PFOMA), and poly(1,1,2,2-tetrahydroperfluorooctyl methacrylate) (PTAN). (* : the overall extent of branching in the PFOMA side chain is 22 ± 5%) [29].

for highly sorbing samples and are less than the hydration for low sorbing samples. In the less hydrated regions, polymer–water and polymer–ion interactions depressed salt solubility in the hydrogels. The structural state of water in polymers and its influence on the solubility, diffusivity and permeability of solutes has been widely studied [6–27]. Using a three-state model for water in polymer gels, Wisniewski and Kim suggested that inorganic chloride salts partition primarily into and are transported through bulk water regions within the polymer gels [18]. Non-freezing water, which is strongly associated with hydrophilic groups in the polymer, has selectivity for solutes such as NaCl, while the properties of freezing water are similar to those of pure bulk water [15,17,25].

This paper reports the salt uptake and transport properties of non-porous block copolymers based on low surface energy fluoropolymers and highly hydrophilic hydrocarbon-based polymers. Incorporation of hydrophilic units into the fluoropolymer backbone leads to microphase-separated block copolymers having high water uptake and high water flux [28]. The fluorinated hydrophobic segments may provide low surface energy, minimally adhesive sites to reduce fouling, while the hydrophilic segments self-assemble to form hydrophilic channels for water permeation through the membrane. In this study, solubility and diffusivity of NaCl are reported for dense films in a systematic series of di- and triblock copolymers composed of hydrophilic poly(2-dimethylaminoethyl methacrylate) (PDMAEMA) and either poly(1,1′-dihydroperfluorooctyl methacrylate) (PFOMA) or poly(1,1,2,2-tetrahydroperfluorooctyl acrylate) (PTAN). The primary chemical structures of the homopolymer constituents of these copolymers are presented in Fig. 1. Sodium chloride is used as a marker solute to probe the effect of morphology and polymer composition on transport properties.

2. Experimental

2.1. Materials

The synthesis and characterization of diblock and triblock copolymers has been presented elsewhere [28]. PFOMA has a branched side chain structure with 22 ± 5% chain branching (i.e. approximately one out of every five side chains contains a fluorinated methyl branch), which frustrates side chain crystallization [29]. In contrast, PTAN has linear but polydisperse side chains that exhibit side chain crystallization [29,30]. The PDMAEMA content and molecular weight of the copolymers are summarized in Table 1. Dense films with uniform thicknesses of 40–180 μm were cast from 5–10% (w/v) polymer solution onto teflon plates at ambient temperature. The solvents for PFOMA- and PTAN-based copolymers were 1,1,2-trichlorotrifluoroethane (i.e. Freon 113) and α,α,α-trifluorotoluene, respectively. Ultrapure water used in this study was produced by a water purification system manufactured by Milllipore Corporation (Bedford, MA). This system consists of two prefilters (5 μ and carbon) followed by a Rios 16 reverse osmosis unit and a Milli-Q Plus TOC ultrapure water purification system in series. Sodium chloride was purchased from Fisher Scientific (Norcross, GA) and was used as received.

2.2. Water uptake measurements

The amount of water sorbed by a sample was determined

Table 1
PDMAEMA content and molecular weights of the synthesized block copolymers. Data were taken from Ref. [28]

Block copolymers	PDMAEMA content		Molecular weight, M_n	
	(wt%)	(mol%)	PDMAEMA (kg/mol)	PFOMA or PTAN (kg/mol)
PDMAEMA-*b*-PFOMA	26	52	29	111
	29	55	27	94
	40	67	32	79
	42	69	29	69
PFOMA-*b*-PDMAEMA-*b*-PFOMA	32	59	42	120 (60 for each block)
PTAN-*b*-PDMAEMA-*b*-PTAN	ca. 38	69	46	110 (55 for each block)

by immersing it in ultrapure water, blotting it between two pieces of filter paper, and weighing it. As water desorbs rapidly, the weighing process was completed within ca. 10 s to minimize experimental error. After each measurement, the film was again immersed in water, and the procedure was repeated until equilibrium water sorption was attained. The water uptake and approximate total hydration (H) were determined from:

$$\text{water uptake} = \frac{W_{wet} - W_{dry}}{W_{dry}} \times 100 \quad (1)$$

and

$$H = \frac{W_{wet} - W_{dry}}{W_{wet}} \quad (2)$$

where W_{wet} and W_{dry} are the weights of a water-swollen film at equilibrium and a dry film, respectively. Hydration is typically defined based on the volume of wet and dry films [4,5]. However, the volume fraction of water in hydrogels is frequently similar to the weight fraction, and therefore, hydration is often approximated as the weight fraction of water in the polymer. Average values of water uptake and hydration are reported for each copolymer composition.

2.3. Differential scanning calorimetry

Differential scanning calorimetry (DSC) was used to estimate the amounts of freezing and non-freezing water in water-swollen dense films at equilibrium [6,9,14–16,19–22,24–27], using a procedure reported previously [31]. These measurements were performed using a Perkin–Elmer DSC-7 operated at a heating rate of 10°C/min. The samples were maintained in an argon atmosphere during measurements, and the temperature range explored was from −150 to 25°C. On the basis of the results from these measurements, the masses of freezing water (W_{fw}) and non-freezing water (W_{nfw}) were determined. The mass of freezing water was calculated from:

$$W_{fw} = Q^h/\Delta H \quad (3)$$

where Q^h, the energy absorbed during melting, was calculated from the peak area of the DSC curve. The latent enthalpy of melting per unit mass of freezing water, ΔH, was assigned a value of 334 J/g, the enthalpy of melting of pure water at 0°C [31]. The mass of non-freezing water, W_{nfw}, was estimated by subtracting the weight of freezing water (W_{fw}) from the total weight of water sorbed in the sample (W_{total}):

$$W_{nfw} = W_{total} - W_{fw} \quad (4)$$

2.4. Kinetic salt desorption measurements

The partition and diffusion coefficients of NaCl were determined from kinetic desorption experiments. In each experiment, a dense polymer film was equilibrated in a 5 wt% aqueous NaCl solution at 25°C. The sample was then removed from the equilibrating solution, wiped to remove excess surface salt, and immersed in a fixed volume of deionized pure water maintained at 25°C. The solution was stirred vigorously to reduce boundary layer resistances to mass transfer. The optimal stirring rate was determined by performing control diffusion experiments using cellulose acetate and verifying that our values for salt partition and diffusion coefficients were in excellent agreement with the literature. As salt desorbed from the film, the conductivity was monitored as a function of time using a Fisher Scientific Model 09-326-2 conductivity meter. Conductivity was converted to mass of salt desorbed via a calibration curve. The salt solubility was determined from the total amount of salt released to the initially salt-free solution, while salt diffusion coefficients were determined from the kinetics of solution conductivity increase.

3. Results and discussion

3.1. State of water in copolymers

The glass transition temperatures (T_g) of the anhydrous homopolymers are 21°C for PDMAEMA [28] and 50°C for PFOMA [33]. The T_g for PTAN should be similar to that of poly(1,1′-dihydroperfluorooctyl acrylate) (−10°C) [33]. However, the high degree of crystallinity of the PTAN side chains makes it difficult to detect T_g. The melting point of PTAN is ca. 80°C [28]. Because the difference between the glass transition temperatures of PDMAEMA and PFOMA is only 30°C, it was difficult to determine the T_g of each phase in the di- and triblock copolymers by DSC. Transmission electron microscopy (TEM) micrographs indicate that the di- and triblock copolymers are microphase-separated [28]. The PDMAEMA-*b*-PFOMA samples (containing 55 and 67 mol% PDMAEMA) have irregular cylindrical morphologies, while the triblock copolymers (i.e. PFOMA-*b*-PDMAEMA-*b*-PFOMA and PTAN-*b*-PDMAEMA-*b*-PTAN) exhibit cylindrical and lamellar morphologies, respectively. The PTAN-*b*-PDMAEMA-*b*-PTAN copolymers are the only ones studied for which the fluoropolymer domains can crystallize.

Fig. 2 presents water uptake and hydration, H, at 25°C for the block copolymers as a function of PDMAEMA concentration. PDMAEMA is water soluble, while PFOMA and PTAN are highly hydrophobic. The water uptake of PFOMA and PTAN is very low (1–2 wt%). As the PDMAEMA content of the PDMAEMA-*b*-PFOMA samples increases, water uptake and total hydration increase. Sharp increases in water uptake and hydration were observed at PDMAEMA contents greater than 60 mol%. Interestingly, triblock copolymers had different water uptake and hydration values than diblock copolymers with similar PDMAEMA content. The PFOMA-*b*-PDMAEMA-*b*-PFOMA and PTAN-*b*-PDMAEMA-*b*-PTAN triblock copolymers sorbed approximately 50% less and 40% more

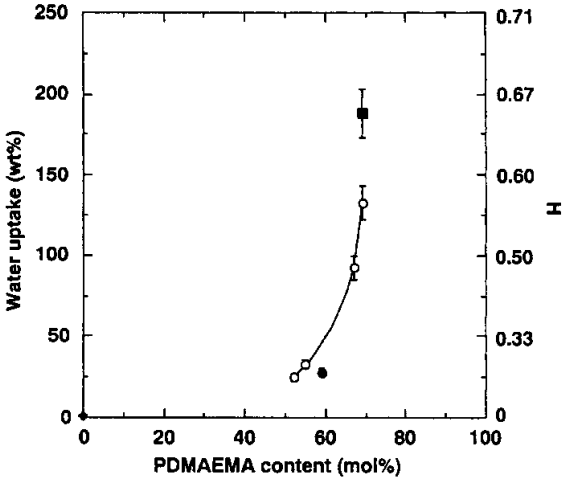

Fig. 2. Total water uptake and total hydration, H, of PFOMA (◆), PTAN (◆), PDMAEMA-*b*-PFOMA (○), PFOMA-*b*-PDMAEMA-*b*-PFOMA (●), and PTAN-*b*-PDMAEMA-*b*-PTAN (■) as a function of PDMAEMA content at 25°C.

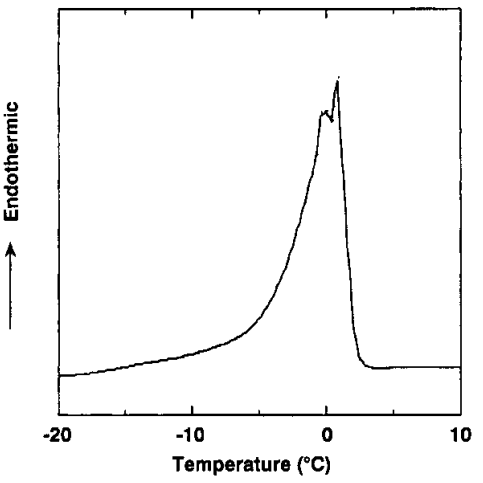

Fig. 3. DSC curve of a PDMAEMA-*b*-PFOMA film (PDMAEMA content: 67 mol%) that has been equilibrated in water. Water uptake: 93 wt% at 25°C ($H = 0.48$). Heating rate: 10°C/min.

water than PFOMA diblock copolymers of similar PDMAEMA composition, respectively. This result may be related to differences in accessibility of the hydrophilic domains of PDMAEMA in block copolymers, which possess different architectures, morphologies and abilities of the fluorinated segments to crystallize.

Fig. 3 presents a representative DSC curve for a PDMAEMA-*b*-PFOMA film (PDMAEMA: 67 mol%) that has been equilibrated in water. Two freezing water peaks were observed near 0°C. On the basis of the three state model of water in hydrophilic polymers (i.e. bulk or free water, interfacial water and bound water), the higher melting peak is ascribed to bulk water, and the lower melting peak is attributed to weakly bound interfacial water [6–27]. Differences in the two types of freezing water have been studied for random copolymers and crosslinked hydrogels [14,15,19–22,24,25]. For most polymers, the bulk free water and weakly bound interfacial water peaks overlap one another significantly, thereby compromising an accurate determination of the amount of each type of water. This problem usually becomes more severe as hydration decreases. Therefore, to compare samples with a wide range of hydration values, it is common to report overall freezing water values (i.e. bulk or free water plus interfacial water). This two state model based on DSC analyses (freezing water and non-freezing water) was used in this study. Higuchi and Iijima discuss the suitability of this model to describe transport of solutes in hydrogels [25].

The total sorbed water concentration as well as the amounts of freezing water and non-freezing water increased with increasing hydrophilic content in hydrolyzed poly(4-acetoxystyrene) [21] and in random copolymers of styrenesulfonic acid and methyl methacrylate [27]. In contrast, the amount of non-freezing water was independent of hydrophilic content in crosslinked poly(vinylalcohol-*co*-itaconic acid) [26] and in crosslinked poly(2-hydroxyethyl methacrylate) [20]. The freezing water content usually increases with increasing total water content [15,20,21,26,27]. Similar trends for bound and free water were observed by proton NMR spectroscopy of poly(2-hydroxyethyl methacrylate) hydrogels: the mole fraction of bound water decreased with increasing total water content [13].

As indicated in Fig. 2, the total amount of water sorbed increases with increasing PDMAEMA content. The fraction of freezing water is presented as a function of PDMAEMA content and total water uptake in Fig. 4a and b, respectively. The fraction of water that is present as freezing water increases with increasing hydrophilic content for PFOMA-based copolymers as shown in Fig. 4a. This behavior is similar to that observed in hydrolyzed poly(4-acetoxystyrene) [21] and in random copolymers of styrenesulfonic acid and methyl methacrylate [27]. The freezing water fraction in the PTAN-*b*-PDMAEMA-*b*-PTAN film is markedly lower than that in a PDMAEMA-*b*-PFOMA film of similar composition. The lamellar morphology of the PTAN-*b*-PDMAEMA-*b*-PTAN film may permit stronger PDMAEMA–water interactions than the irregular cylindrical morphology of the PDMAEMA-*b*-PFOMA films [28]. As indicated in Fig. 4b, the fraction of freezing water in the polymers was not strongly correlated with total water uptake. Although water uptake increases with increasing hydrophilic content for several other random copolymers and crosslinked hydrogels [21,26,27], hydrophilic content alone is not a good indicator for total water uptake for our microphase-separated block copolymers (cf. Fig. 2). Apparently, a subtle interplay between copolymer chemical content and morphology influences total water uptake and freezing water content in these block copolymers.

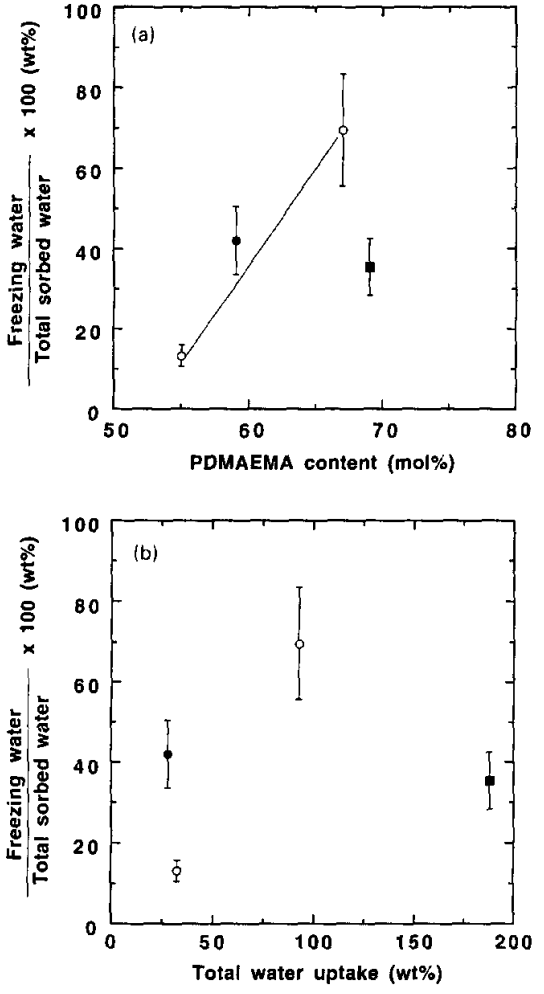

Fig. 4. (a) Percentage of freezing water in PDMAEMA-*b*-PFOMA (○), PFOMA-*b*-PDMAEMA-*b*-PFOMA (●) and PTAN-*b*-PDMAEMA-*b*-PTAN (■) as a function of PDMAEMA content at 25°C. (b) Percentage of freezing water in PDMAEMA-*b*-PFOMA (○), PFOMA-*b*-PDMAEMA-*b*-PFOMA (●) and PTAN-*b*-PDMAEMA-*b*-PTAN (■) as a function of total water uptake at 25°C.

3.2. Salt solubility

Fig. 5 presents the relationship between the salt partition coefficient, *k*, and PDMAEMA content at 25°C. The salt partition coefficient of PDMAEMA-*b*-PFOMA films increases with increasing PDMAEMA content. The salt partition coefficient of PTAN-*b*-PDMAEMA-*b*-PTAN is similar to that of PFOMA diblock copolymers with similar PDMAEMA content. The salt partition coefficient of the PFOMA-*b*-PDMAEMA-*b*-PFOMA film, however, is about half the value of a PDMAEMA-*b*-PFOMA film of similar hydrophilic (i.e. PDMAEMA) content. On the basis of these results, hydrophilic content is not the only variable influencing salt solubility. Other factors, such as morphology and amount of freezing water, may also influence salt solubility values. These issues are discussed in more detail below.

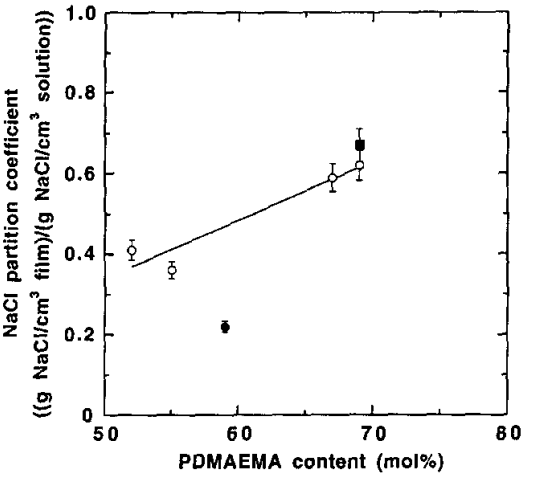

Fig. 5. Sodium chloride partition coefficients for PDMAEMA-*b*-PFOMA (○), PFOMA-*b*-PDMAEMA-*b*-PFOMA (●) and PTAN-*b*-PDMAEMA-*b*-PTAN (■) as a function of PDMAEMA content at 25°C.

Yasuda et al. reported that the salt partition coefficient should be equal to the hydration if there are no strong polymer–water interactions [4]. In this case, the concentration of the salt solution sorbed in the polymer is equal to that of the bulk salt solution. Experimentally, salt partition coefficients are nearly equal to the hydration for highly sorbing samples (e.g. hydrogels) and are often lower than the hydration for low sorbing samples. Yoon and Jhon reported that NaCl partitioned only into the water-containing regions of cross-linked poly(2-hydroxyethyl methacrylate) membranes [20]. Water uptake values for hydrophobic PFOMA and PTAN are only 1–2 wt%. Therefore, water sorbs almost exclusively into the hydrophilic PDMAEMA domains of these microphase-separated block copolymers.

Fig. 6 presents the salt partition coefficient as a function of the effective hydration, H_{eff}, which is estimated as the weight fraction of water sorbed into the hydrophilic PDMAEMA domains of the copolymers. The effective hydration is estimated by assuming that all of the sorbed water is confined to the hydrophilic PDMAEMA regions of the copolymers and has units of mass of water sorbed per mass of PDMAEMA in the copolymer. As the effective hydration increases, the salt partition coefficient increases in PDMAEMA-*b*-PFOMA films. All salt partition coefficients lie below the line $k = H_{eff}$, suggesting that polymer–salt interactions influence the overall salt solubility in the copolymer. The ratio of the partition coefficient to effective hydration is plotted as a function of effective hydration in Fig. 7. This ratio is approximately constant for PDMAEMA-*b*-PFOMA samples, suggesting that water–salt–polymer interactions in PFOMA diblock copolymers are similar to each other. The value of k/H_{eff} for PTAN-*b*-PDMAEMA-*b*-PTAN is similar to that of the PFOMA diblock copolymers. However, the k/H_{eff} value shown in Fig. 7 for PFOMA-*b*-PDMAEMA-*b*-PFOMA is about half that of PDMAEMA-*b*-PFOMA of

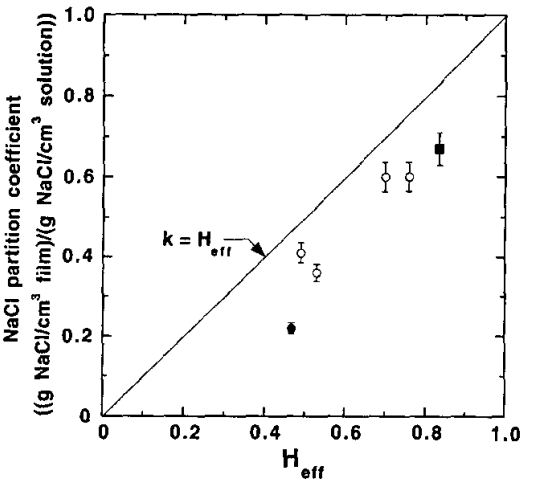

Fig. 6. Sodium chloride partition coefficients for PDMAEMA-*b*-PFOMA (○), PFOMA-*b*-PDMAEMA-*b*-PFOMA (●) and PTAN-*b*-PDMAEMA-*b*-PTAN (■) as a function of effective hydration, H_{eff}, at 25°C. Effective hydration is calculated by assuming that all sorbed water is confined to the hydrophilic domains of the polymer.

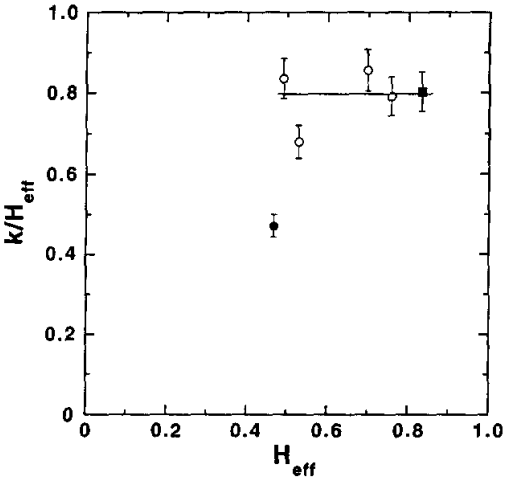

Fig. 7. Ratio of sodium chloride partition coefficient, k, to effective hydration, H_{eff}, in PDMAEMA-*b*-PFOMA (○), PFOMA-*b*-PDMAEMA-*b*-PFOMA (●) and PTAN-*b*-PDMAEMA-*b*-PTAN (■) as a function of effective hydration at 25°C. Effective hydration is calculated by assuming that all sorbed water is confined to hydrophilic domains.

similar composition. Yasuda et al. reported k/H values of 0.44–1.12 for various hydroxyalkyl methacrylate based hydrogels [4]. The values in Fig. 7 are consistent with their results.

Wisniewski and Kim proposed that inorganic chloride salts partition primarily into the bulk water regions of crosslinked poly(2-hydroxyethyl methacrylate), suggesting that ion partitioning and transport occur primarily in regions rich in bulk water [18]. In this regard, Fig. 8 presents k as a function of corrected hydration, H^*, which is estimated as the weight fraction of *freezing* water sorbed in PDMAEMA domains. The salt partition coefficients for the highly sorbing copolymers are in excellent agreement with the relationship $k = H^*$, suggesting that the amount of freezing water (i.e. water which has no strong interactions with polymer segments) strongly influences the salt solubility in highly hydrated samples of these copolymers. The sample with the lowest corrected hydration, a PDMAEMA-*b*-PFOMA sample containing 55 mol% PDMAEMA, deviates from this relation, implying that salt sorption in relatively weakly hydrated samples may be influenced by polymer–water and polymer–ion interactions. Like conventional crosslinked hydrogels, the partition coefficient of NaCl for these heterophase materials depends primarily on the freezing water content of the hydrophilic PDMAEMA domains in the phase-separated block copolymers.

3.3. Salt diffusivity

Salt diffusion coefficients, D, for the block copolymers were determined using a Fickian analysis for desorption from a plane sheet [32]. The volume of initially pure water into which the salt is desorbing is finite. However, the volume of water is sufficiently large and the amount of salt desorbing is sufficiently small that the salt concentration in the desorption cell does not influence the results. Values of D were estimated from the kinetic desorption data in the region where the fractional desorption, M_t/M_∞, is a linear function of $t^{1/2}$. The following equation was used to calculate diffusion coefficients:

$$\frac{d(M_t/M_\infty)}{d(t^{1/2})} = \frac{4}{\ell}\left(\frac{D}{\pi}\right)^{1/2} \tag{5}$$

where ℓ is polymer film thickness, t is time, and M_t and M_∞ are the masses of penetrant in the polymer at time t, and at the beginning of the experiment, respectively. Values of D were estimated for short times, corresponding to values of $M_t/M_\infty < 0.6$. The uncertainties in the diffusion coefficients were estimated using a propagation of error analysis and were found to be ca. 10% [34].

Fig. 9 is a representative salt kinetic desorption curve for a PTAN-*b*-PDMAEMA-*b*-PTAN film (69 mol% PDMAEMA). A short induction period is observed for $t^{1/2} < 5\ s^{1/2}$. This phenomenon is ascribed to delays associated with conductivity meter response and the time required to establish a zero-concentration boundary condition at the film surface when the film is introduced into the water and the experiment is started. On the basis of control experiments, in which an initially salt-free solution is spiked suddenly with a small aliquot of salt solution, these factors are expected to last approximately 10 s or less. Another possible source of delay in the beginning of diffusion-controlled release of salt from the polymer film is the unique morphological structure of these materials. The hydrophilic PDMAEMA microdomains are sandwiched in a matrix of

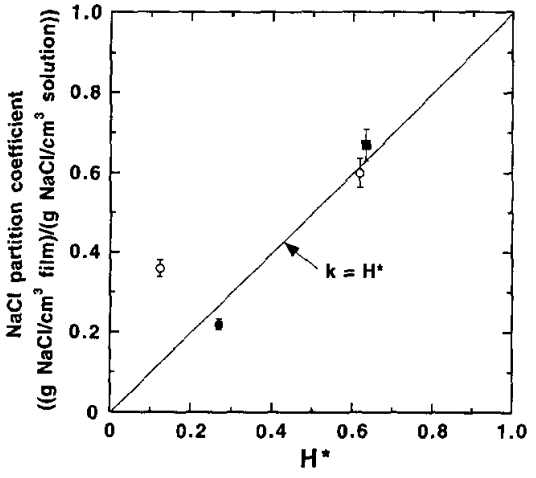

Fig. 8. Sodium chloride partition coefficient in PDMAEMA-*b*-PFOMA (○), PFOMA-*b*-PDMAEMA-*b*-PFOMA (●) and PTAN-*b*-PDMAEMA-*b*-PTAN (■) as a function of corrected hydration, H^*, at 25°C. Hydration was corrected to include only the amount of freezing water present in hydrophilic domains.

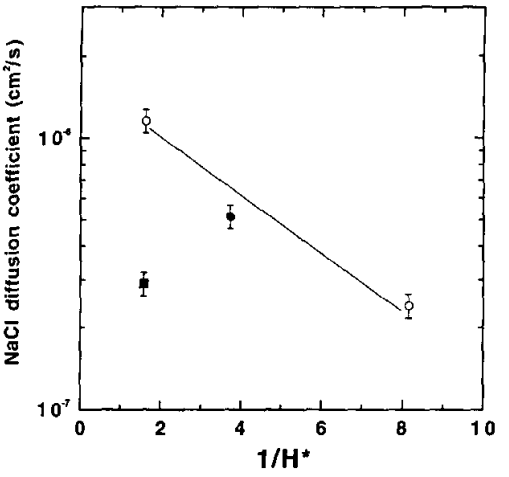

Fig. 10. Sodium chloride diffusion coefficient in PDMAEMA-*b*-PFOMA (○), PFOMA-*b*-PDMAEMA-*b*-PFOMA (●) and PTAN-*b*-PDMAEMA-*b*-PTAN (■) as a function of corrected hydration, H^*, at 25°C.

hydrophobic PTAN microdomains. This structure may lead to some induction period as the concentration gradients inside the film for Fickian-dominated mass transport are established.

Systematic correlations between salt diffusivity and hydrophilic content of the polymers are not observed. Previous studies report, in qualitative agreement with free volume theory, that salt diffusivity decreases exponentially with decreasing reciprocal hydration in cellulose acetate [3] and in a variety of hydroxyalkyl methacrylate (e.g. hydroxyethyl methacrylate, HEMA)-based hydrogels [4,5]. However, our data do not exhibit a simple, systematic change in salt diffusion coefficients with either reciprocal hydration or reciprocal effective hydration. However, when the hydration is corrected to include only the weight fraction of freezing water in the hydrophilic domains, then the salt diffusivity of PFOMA-based copolymers decreases linearly with increasing $1/H^*$ as shown in Fig. 10. Presumably, freezing water is more mobile than non-freezing water and can more effectively assist in salt transport. Salt diffusion coefficients vary by a factor of approximately 50 among the various copolymers considered in this study. The PTAN-*b*-PDMAEMA-*b*-PTAN film has a much lower salt diffusion coefficient than PFOMA-based copolymer films with similar values of $1/H^*$, suggesting that other factors, such as morphology, also influence salt diffusion. All of the PFOMA-based copolymers exhibit some form of cylindrical morphology, and the morphology of PTAN-*b*-PDMAEMA-*b*-PTAN is lamellar [28]. This change in morphology may result in a different tortuosity factor for PTAN-*b*-PDMAEMA-*b*-PTAN than for the other copolymers.

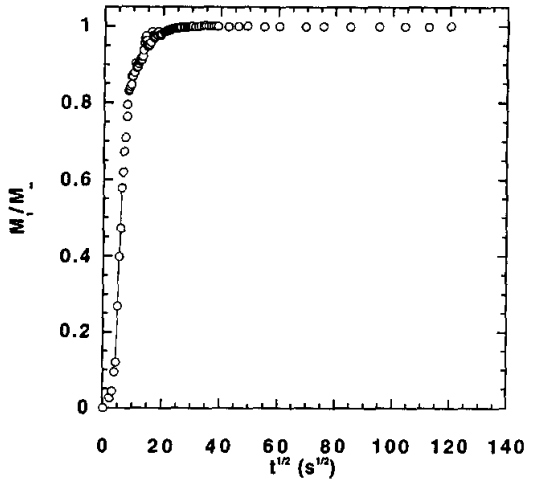

Fig. 9. Kinetic desorption of sodium chloride from PTAN-*b*-PDMAEMA-*b*-PTAN film (PDMAEMA content: 69 mol%) at 25°C. The film thickness is 50 μm, and the straight line through the experimental data is the best fit of Eq. (5) to the data from $0.1 < M_t/M_\infty < 0.6$, which yields a salt diffusivity of 2.9×10^{-7} cm²/s.

To underscore the impact of freezing water content on salt diffusivity, Fig. 11 presents a correlation of salt diffusivity and the fraction of freezing water in the sample. Interestingly, for the PFOMA-based copolymers, salt diffusivity increases as the amount of freezing water increases. The freezing water presumably has weaker interactions with the hydrophilic sites in the polymer backbone and is readily accessible to assist in salt transport. In contrast to the results reported previously for hydroxyalkyl methacrylate-based hydrogels [4], the salt diffusion coefficients of PDMAEMA copolymers do not depend simply on the total hydration. Instead, they are correlated with the freezing water content of the hydrophilic domains. Hence, the state of water in the

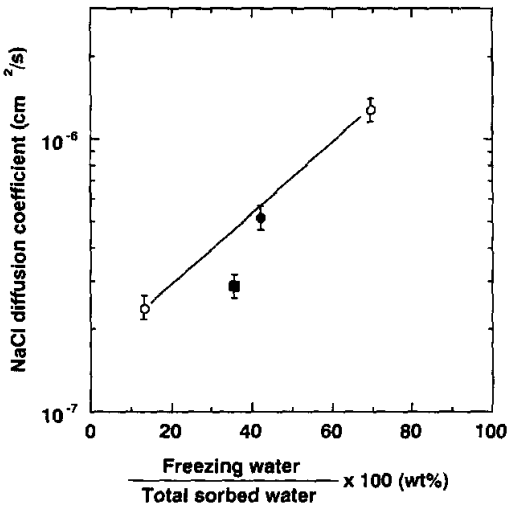

Fig. 11. Sodium chloride diffusion coefficient in PDMAEMA-*b*-PFOMA (○), PFOMA-*b*-PDMAEMA-*b*-PFOMA (●) and PTAN-*b*-PDMAEMA-*b*-PTAN (■) as a function of the percentage of freezing water at 25°C.

phase-separated block copolymers is an important factor influencing salt transport.

4. Conclusions

Solubility and diffusivity of NaCl were determined in dense films of microphase-separated block copolymers composed of poly(2-dimethylaminoethyl methacrylate) (PDMAEMA) and either poly(1,1′-dihydroperfluorooctyl methacrylate) (PFOMA) or poly(1,1,2,2-tetrahydroperfluorooctyl acrylate) (PTAN). PDMAEMA is water soluble, while PFOMA and PTAN are highly hydrophobic. As PDMAEMA content (i.e. hydrophilic content) of PDMAEMA-*b*-PFOMA diblock copolymers increases, total water uptake and hydration increase. The salt partition coefficients also increase with increasing PDMAEMA content and effective hydration. In contrast, salt diffusivity does not correlate well with increasing PDMAEMA content and effective hydration.

Triblock copolymers (i.e. PTAN-*b*-PDMAEMA-*b*-PTAN and PFOMA-*b*-PDMAEMA-*b*-PFOMA) have different values of total water uptake, hydration, salt partition, and diffusion coefficients than those of PFOMA diblock copolymers with the same mole percent of hydrophilic PDMAEMA in the chain backbone. However, regardless of polymer morphology, salt partition and diffusion coefficients of these phase-separated block copolymers are well correlated with the percentage of freezing water in the sample.

Acknowledgements

This work was supported in part by the Office of Naval Research, the National Water Research Institute and the American Water Works Association Research Foundation. We also gratefully acknowledge partial support from the STC program of the National Science Foundation under Agreement No. CHE9876674.

References

[1] Riley RL. Reverse osmosis. In: Baker RW, Cussler EL, Eykamp W, Koros WJ, Riley RL, Strathmann H, editors. Membrane separation systems: recent developments and future directions. Park Ridge, NJ: Noyes Data Corporation, 1991. p. 276–327.
[2] Hamza A, Pham VA, Matsuura T, Santerre JP. J Membr Sci 1997; 131(1–2):217–27.
[3] Rosenbaum S, Mahon HI, Cotton O. J Appl Polym Sci 1967; 11(10):2041–65.
[4] Yasuda H, Lamaze CE, Ikenberry LD. Makromol Chem 1968; 118(2858):19–35.
[5] Yasuda H, Ikenberry LD, Lamaze CE. Makromol Chem 1969; 125(3062):108–18.
[6] Magne FC, Portas HJ, Wakeham H. J Am Chem Soc 1947; 69(8):1896–902.
[7] Drost-Hansen W. Ind Engng Chem 1969;61(11):10–47.
[8] Ogiwara Y, Kubota H, Hayashi S, Mitomo N. J Appl Polym Sci 1970;14(2):303–9.
[9] Frommer MA, Lancet D. J Appl Polym Sci 1972;16(5):1295–303.
[10] Jhon MS, Andrade JD. J Biomed Mater Res 1973;7(6):509–22.
[11] Carles JE, Scallan AM. J Appl Polym Sci 1973;17(6):1855–65.
[12] Krishnamurthy S, McIntyre D, Santee ER, Wilson CW. J Polym Sci, Part B: Polym Phys 1973;11(3):427–48.
[13] Lee HB, Andrade JD, Jhon MS. Polym Prepr (Am Chem Soc Div Polym Chem) 1974;15(1):706–11.
[14] Lee HB, Jhon MS, Andrade JD. J Colloid Interf Sci 1975;51(2):225–31.
[15] Taniguchi Y, Horigome S. J Appl Polym Sci 1975;19(10):2743–8.
[16] Nelson RA. J Appl Polym Sci 1977;21(3):645–54.
[17] Toprak C, Agar JN, Falk M. J Chem Soc, Faraday Trans 1 1979;75(4):803–15.
[18] Wisniewski S, Kim SW. J Membr Sci 1980;6(3):299–308.
[19] Nakamura K, Hatakeyama T, Hatakeyama H. Text Res J 1981; 51(9):607–13.
[20] Yoon SC, Jhon MS. J Appl Polym Sci 1982;27(8):3133–49.
[21] Nakamura K, Hatekeyama T, Hatakeyama H. Polymer 1983; 24(7):871–6.
[22] Higuchi A, Komiyama J, Iijima T. Polym Bull 1984;11(2):203–8.
[23] Higuchi A, Abe M, Komiyama J, Iijima T. J Membr Sci 1984; 21(2):113–21.
[24] Higuchi A, Iijima T. Polymer 1985;26(1207):1207–11.
[25] Higuchi A, Iijima T. Polymer 1985;26(12):1833–7.
[26] Higuchi A, Fushima H, Iijima T. J Membr Sci 1985;25(2):171–80.
[27] Nakagawa T, Sakurada T. Kobunshi Ronbunshu 1986;43(11):819–25.
[28] Arnold ME, Nagai K, Freeman BD, Spontak RJ, Leroux D, Betts D, DeSimone JM. To be submitted to Macromolecules.
[29] Kassis CM, Steehler JK, Betts DE, Guan Z, Romack TJ, DeSimone JM, Linton RW. Macromolecules 1996;29(9):3247–54.
[30] Banks RE, Smart BE, Tatlow JC. Organofluorine chemistry: principles and commercial applications. New York: Plenum Press, 1994.
[31] Hirata Y, Mirata Y, Nakagawa T. J Membr Sci 1999;163(2):357–66.
[32] Crank J. The mathematics of diffusion. Oxford: Clarendon Press, 1989. p. 44–68.
[33] Arnold ME, Nagai K, Freeman BD, Spontak RJ, Betts DE, DeSimone JM, Pinnau I. Macromolecules 2001;34(16):5611–9.
[34] Bevington PR, Robinson DK. Data reduction and error analysis for the physical sciences. 2nd ed. New York: McGraw-Hill, 1992.

Gas Permeation Properties of Poly(1,1′-dihydroperfluorooctyl acrylate), Poly(1,1′-dihydroperfluorooctyl methacrylate), and Poly(styrene)-*b*-poly(1,1′-dihydroperfluorooctyl acrylate) Block Copolymers

Michelle E. Arnold, Kazukiyo Nagai,† Benny D. Freeman,* and Richard J. Spontak

Department of Chemical Engineering, North Carolina State University, Raleigh, North Carolina 27695-7905

Douglas E. Betts‡ and Joseph M. DeSimone§

Department of Chemistry, University of North Carolina at Chapel Hill, Chapel Hill, North Carolina 27599-3290

Ingo Pinnau

Membrane Technology and Research, Inc., 1360 Willow Road, Suite 103, Menlo Park, California 94025-1516

Received February 27, 2001; Revised Manuscript Received May 17, 2001

ABSTRACT: The permeabilities of rubbery poly(1,1′-dihydroperfluorooctyl acrylate) (PFOA), glassy poly(1,1′-dihydroperfluorooctyl methacrylate) (PFOMA), and poly(styrene)-*b*-poly(1,1′-dihydroperfluorooctyl acrylate) (PS-*b*-PFOA) diblock copolymers to N_2, O_2, H_2, CH_4, C_2H_6, and CO_2 at 446 kPa and to C_3H_8 at 308 kPa are reported as a function of temperature. In general, PFOMA has lower fractional free volume, smaller gas permeability coefficients, and larger activation energies of permeation than PFOA, consistent with the more restricted long-range segmental mobility of PFOMA. The PS-*b*-PFOA copolymers exhibit complex microphase-separated morphologies, and their gas permeability coefficients are intermediate between those of glassy PS and rubbery PFOA, decreasing in magnitude with increasing PS content.

Introduction

Typically, fluoropolymers have high thermal, chemical, and oxidative stability, which suggests that they could be attractive membrane materials for separations in chemically challenging environments, such as vapor separation or removal of perfluorocarbons from waste streams containing hydrofluoric acid. Traditionally, however, fluoropolymers have been synthesized and processed in solvents such as chlorofluorocarbons (CFCs) and halocarbons, which are deleterious to the environment.[1-3] To address this problem, DeSimone and coworkers[1,4] have developed methods for the synthesis of fluoropolymers in supercritical carbon dioxide ($scCO_2$). Two chemically related fluoropolymers—poly(1,1′-dihydroperfluorooctyl acrylate) (PFOA) and poly(1,1′-dihydroperfluorooctyl methacrylate) (PFOMA)—have been synthesized in $scCO_2$ for this study, and their chemical structures are presented in Figure 1. At ambient temperature, PFOA is a rubbery polymer with a glass transition temperature, T_g, of −10 °C,[5] while PFOMA is a glassy polymer with a T_g of 50 °C.

Block copolymers offer an extra degree of freedom in tailoring polymer properties.[6,7] Only a limited number of gas permeation studies employing block copolymers have been reported in the literature.[8-18] This work describes the permeation and morphological characteristics of a series of microphase-separated poly(styrene)-*b*-poly(1,1′-dihydroperfluorooctyl acrylate) (PS-*b*-PFOA)

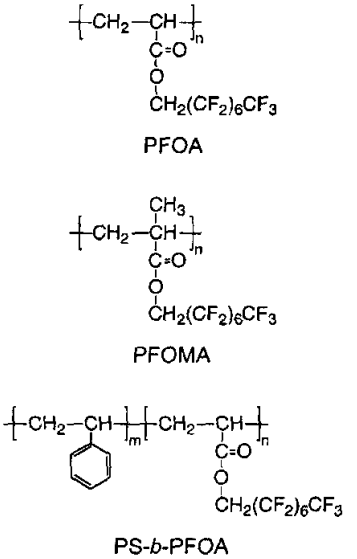

Figure 1. Chemical structures of the poly(1,1′-dihydroperfluorooctyl acrylate) (PFOA) and poly(1,1′-dihydroperfluorooctyl methacrylate) (PFOMA) homopolymers as well as the poly(styrene-*b*-1,1′-dihydroperfluorooctyl acrylate) (PS-*b*-PFOA) diblock copolymers.

* To whom correspondence should be addressed.
† Present address: CSIRO Molecular Science, Private Bag 10, Clayton South, VIC 3169, Australia.
‡ Present address: Nalco Chemical Company, One Nalco Center, Naperville, IL 60563-1198.
§ Also affiliated with Department of Chemical Engineering, North Carolina State University, Raleigh, NC 27695-7905.

10.1021/ma010355i CCC: $20.00
Published on Web 07/06/2001

diblock copolymers and compares them with the properties of the constituent homopolymers, PFOA and PS, and with those of a structurally related fluoropolymer, PFOMA.

Background

Transport Fundamentals. The permeability, P, of a polymer film of thickness l to a penetrant is[19]

$$P = \frac{Nl}{p_1 - p_2} \quad (1)$$

where N is the steady-state penetrant flux, and p_1 and p_2 denote the upstream and downstream penetrant partial pressures, respectively. Permeation through dense, nonporous polymer films is conventionally described by the solution-diffusion model,[20] in which penetrant molecules first sorb into the upstream face of the film, diffuse through the polymer matrix, and then desorb from the downstream face of the film. The rate-limiting step in this process is diffusion across the polymer film. Within the context of this transport model and when $p_2 \ll p_1$, permeability is given by[19]

$$P = DS \quad (2)$$

where D is the concentration-averaged effective diffusion coefficient, and S is the apparent solubility coefficient (i.e., the ratio of the dissolved penetrant concentration in the upstream face of the film to the upstream penetrant partial pressure in the contiguous gas phase). A measure of the ability of a polymer matrix to separate gaseous penetrants is given by the ideal selectivity for penetrant A relative to penetrant B (α_{AB}):[19]

$$\alpha_{AB} = \frac{P_A}{P_B} \quad (3)$$

where P_A and P_B are the permeability coefficients of species A and B, respectively.

Effect of Temperature on Permeability. Permeability coefficients usually obey an Arrhenius relationship:[19]

$$P = P_0 e^{-E_P/RT} \quad (4)$$

where P_0 is a constant, E_P is the activation energy of permeation, R is the universal gas constant, and T denotes absolute temperature. If the temperature range of interest is sufficiently far from thermal transitions (e.g., melting, glass−rubber or order−disorder), then E_P is usually independent of temperature. Because permeation includes both diffusion and solution steps, the activation energy of permeation is written as[19]

$$E_P = E_D + \Delta H_s \quad (5)$$

where E_D is the activation energy of diffusion, which describes the energy required to create a diffusion gap of sufficient size to accommodate a penetrant molecule.[21] The overall enthalpy of sorption, ΔH_s, is frequently written in terms of two contributions:[19]

$$\Delta H_s = \Delta H_{cond} + \Delta H_{mix} \quad (6)$$

where ΔH_{cond} is the enthalpy of condensation for the pure penetrant and ΔH_{mix} is the enthalpy required for mixing the penetrant and polymer segments.

Experimental Section

Materials. High-molecular-weight PFOA and PFOMA were synthesized in $scCO_2$ as previously described by Guan et al.[4] Homogeneous free-radical solution polymerization of a fluorinated monomer (e.g., 1,1′-dihydroperfluorooctyl acrylate, FOA) was typically conducted in the presence of 1 wt % azoisobutyronitrile (AIBN) as initiator at 59.4 °C and 207 bar for 48 h.[4] The FOA and FOMA monomers were graciously provided by 3M Co. (Minneapolis, MN), and styrene monomer was purchased from Aldrich Chemical Co. (Milwaukee, WI). The PS-*b*-PFOA copolymers were synthesized by an iniferter process,[5,22,23] in which telechelic polystyrene was first produced using tetraethylthiuram disulfide as the thermal iniferter and characterized. The PFOA block was subsequently polymerized using the telechelic PS as a macroinitiator.[5,24]

Nitrogen, O_2, H_2, CH_4, C_2H_6, C_3H_8, and CO_2 were obtained from National Specialty Gases (Raleigh, NC) and were used as received. The minimum purity of each gas was 99.998 mol % for N_2, 99.8 mol % for H_2, 99.5 mol % for O_2 and CO_2, and 99 mol % for CH_4, C_2H_6, and C_3H_8. In addition, 1,1,2-trichlorotrifluoroethane (Freon-113), used to cast films and prepare composite membranes, was acquired from E.I. DuPont de Nemours and Co. (Wilmington, DE).

Polymer Characterization. For the PS-*b*-PFOA block copolymers, molecular weights for the telechelic polystyrenes were first measured using a Waters 150-CV gel permeation chromatograph equipped with Ultrastyragel columns of 10, 50, 100, and 1000 nm porosities. Tetrahydrofuran was the eluent, and the instrument was calibrated using PS standards from Showa Denko (Tokyo, Japan).[24] The number of *N,N*-diethyldithiocarbamate end groups per polymer chain (i.e., the functionality) of each telechelic polystyrene was ascertained from UV spectrophotometry results acquired using a Perkin-Elmer Lambda 6 UV−vis spectrophotometer.[24] Composition analysis of the PS-*b*-PFOA block copolymers was conducted with proton nuclear magnetic resonance (^{1}H NMR) using a Bruker WM 250 spectrometer.[24] These measurements were performed in a mixed solvent of Freon-113 and either d_2-methylene chloride or d_6-acetone. Subsequently, PFOA block weights were determined using the ratio of the fluorinated block peak to the PS block peak and the known molecular weight of the PS block.[24]

Glass transition temperatures were characterized by differential scanning calorimetry (DSC), using a Perkin-Elmer DSC-7 calorimeter operated at a heating rate of 20 °C/min in a N_2 atmosphere. The density of PFOA was determined from pycnometric analysis, in which the masses and volumes of PFOA films cast from a 20% (w/v) solution in Freon-113 were measured after complete solvent evaporation (quiescent drying at ambient temperature for 3 weeks, followed by vacuum-drying at ambient temperature for 3 days). The density of PFOMA was ascertained by gravimetric analysis, in which PFOMA films measuring ca. 200 μm thick were prepared from similar Freon-113 solutions using a ring-casting technique.[25] Following complete solvent evaporation, the density of PFOMA was estimated from the masses and dimensions of uniform circular PFOMA samples (1.90 cm in diameter).

Morphological Characterization. Electron-transparent specimens for transmission electron microscopy (TEM) were prepared by casting PS-*b*-PFOA films from 5% (w/v) Freon-113 solutions in Teflon molds, followed by slow solvent evaporation. Dried films measuring 0.3−0.6 mm thick were subsequently microtomed at −100 °C in a Reichert-Jung Ultracut-S cryoultramicrotome, and the resultant thin sections were exposed to the vapor of 2% RuO_4(aq) for 5 min to stain the PS-rich microdomains. Images were acquired with a Zeiss EM902 electron spectroscopic microscope operated at 80 kV and energy-loss settings of 0−180 eV. Correlation lengths were discerned from 2D Fourier transforms of digitized negatives using the Digitalmicrograph software package by Gatan Inc. (Pleasanton, CA).

Table 1. Physical Properties of the Polymers Investigated in This Study

	ϕ_S	T_g (°C)	$\bar{M}_n \times 10^{-3}$ PS	PFOA	PFOMA	density (g/cm³)
PFOA	0.0	−10		>10³		1.74
PS-*b*-PFOA	0.12	−6/66	14.0	172		
PS-*b*-PFOA	0.23	−3/67	4.5	24.5		
PS-*b*-PFOA	0.03	−7/69	6.60	349		
PS	1.0	100[a]	>10³			1.06[a]
PFOMA		50			>10³	1.89

[a] Reference 50.

Composite membranes were prepared by coating 1−2% (w/v) Freon-113 solutions onto a highly microporous polysulfone (PSF) support with a nonwoven polyester backing. Thin strips of the composite membranes for scanning electron microscopy (SEM) were cut from areas adjacent to those used for permeation testing. The strips were soaked in ethanol for 1−5 min to swell and open the microporous structure of the PSF support. After the polyester backing was removed, each sample was fractured in liquid nitrogen. The resultant cross sections were mounted and sputter-coated with ca. 20 nm of Au, and backscattered electron images were acquired at 20 kV with a Hitachi S-3200N variable-pressure electron microscope. The separating layer thickness for each composite membrane was estimated on the basis of SEM analysis and represents the average of multiple measurements collected from several samples of each membrane.

Permeation Measurements. Pure gas permeability coefficients of composite membranes were determined using a constant pressure/variable volume method.[26] The feed-side (upstream) pressure was maintained at 446 kPa (50 psig) for all penetrant gases except C_3H_8, which was tested at 308 kPa (30 psig), while the permeate-side (downstream) pressure was atmospheric. Permeation measurements were conducted in ca. 5 °C intervals for temperatures ranging from ambient (23 °C) to 45 °C, and temperature was maintained within ±0.5 °C with a DYNA-SENSE temperature control system (Cole-Palmer, Niles, IL). At each temperature, the typical order of permeation measurements was N_2, O_2, H_2, CH_4, C_2H_6, C_3H_8, CO_2, N_2, O_2. After the fluxes for all penetrant gases were determined at each temperature, the temperature was decreased back to 23 °C, and the fluxes for N_2, O_2, and at least one other penetrant (typically C_2H_6 or C_3H_8) were measured again. Permeate flow rates were determined using a soap film bubble flowmeter from Alltech (Deerfield, IL). Once steady-state conditions were established, the pure gas permeability coefficient, P, was estimated from

$$P = \frac{l}{A(p_l - p_{atm})} \frac{273\ \text{K}}{T} \frac{p_{atm}}{76\ \text{cm Hg}} \left(\frac{dV}{dt}\right)_{ss} \quad (7)$$

where l is the estimated effective separating layer thickness of the membrane (cm), A is the membrane area (cm²), p_{atm} is atmospheric pressure (cmHg), p_l is the upstream pressure (cmHg), T is absolute temperature (K), and $(dV/dt)_{ss}$ is the steady-state volumetric rate of soap-bubble displacement in the flowmeter (cm³/s). All permeability coefficients are reported in units of barrers, where 1 barrer = 10^{-10} cm³ (STP)·cm/(cm²·s·cmHg).

Results and Discussion

Physical Property Characterization. The physical properties of PFOA, PFOMA, and PS homopolymers, as well as three PS-*b*-PFOA diblock copolymers, are recorded in Table 1. High-molecular-weight PFOA is a rubbery polymer with a T_g of −10 °C. In contrast, PFOMA is a glassy polymer with a T_g of 50 °C. The difference in T_g is attributed to the additional methyl group in the PFOMA backbone. Each of the PS-*b*-PFOA copolymers has two T_g values, which is a signature of microphase separation.[27] The lower T_g is associated with the glass transition of chain segments in the PFOA-rich microdomains, while the higher T_g is ascribed to the glass transition of PS-rich microdomains. The T_g associated with the PFOA-rich phase is a few degrees higher than that of pure PFOA, and the T_g associated with the PS-rich phase is 31−34 °C lower than that of pure PS. Differences between the T_g's of the copolymer blocks and those of the parent homopolymers can be attributed to three effects. Interfacial mixing between PS and PFOA microdomains promotes convergence of the two T_g's (until a single T_g would be achieved upon microphase dissolution). Incomplete microphase separation in which the PS microdomains contain PFOA due to kinetic entrapment or polydispersity effects[28] results in residual intramicrodomain mixing and is accompanied by a depression in the T_g associated with the PS-rich phase. In addition, the T_g of a relatively short homopolymer or copolymer block depends sensitively on molecular weight. Lu and Jiang[29] have proposed the following correlation between the T_g of PS and the degree of polymerization (N_S):

$$T_g = \frac{2N_S T_g^\infty}{2N_S + C_\infty f(y)} \quad (8)$$

where T_g^∞ = 373.15 K and C_∞ = 10.68 for PS. The function $f(y)$ is obtained from the wormlike chain model and is given by

$$f(y) = 1 - 3y + 6y^2 - 6y^3(1 - e^{-1/y}) \quad (9)$$

For a vinyl polymer chain,

$$y = \frac{C_\infty}{4N_S \sin^2(\theta/2)} \quad (10)$$

where θ is the angle formed by the C−C single bonds along the backbone (109.5°). On the basis of this model, the T_g values of the PS blocks with $\bar{M}_n$ equal to 14 000, 4500, and 6600 (see Table 1) would be 87, 68, and 76 °C, respectively. Differences between these calculated T_g's and the experimental T_g's, particularly for the samples containing PS blocks of molecular weight 14 000 and 6600, suggest that PS segment molecular weight is insufficient to explain the large depression in glass transition temperatures of the PS in these block copolymers. Therefore, interfacial and/or residual intramicrodomain mixing may also contribute to the reduced T_g values. This issue is revisited later in the discussion.

The densities of PFOA and PFOMA are also included in Table 1. The density of PFOA is 1.74 g/cm³, which is essentially equal to that of TFE/BDD87, a glassy, random perfluorodioxole copolymer prepared from 13 mol % tetrafluoroethylene and 87 mol % 2,2-bis(trifluoromethyl)-4,5-difluoro-1,3-dioxole.[30] In contrast, the density of PFOMA, 1.89 g/cm³, lies between that of TFE/BDD87 and poly(tetrafluoroethylene) (2.15−2.20 g/cm³).[31] The measured densities of PFOA and PS provided in Table 1 are used in conjunction with the known mass-fraction compositions of the PS-*b*-PFOA copolymers (from ^{1}H NMR) to estimate volume fractions of PS (ϕ_S). Insufficient quantities of the PS-*b*-PFOA copolymer samples were available for density determination.

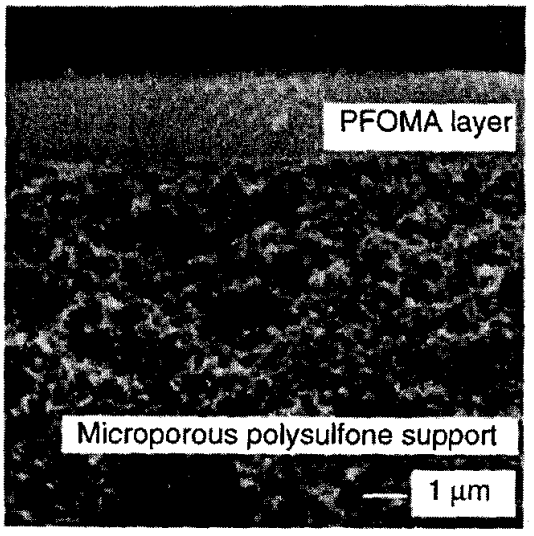

Figure 2. Scanning electron micrograph of a PFOMA composite membrane used for gas permeability measurements. The PFOMA separating layer is approximately 2.1 μm thick and is coated onto a highly microporous polysulfone support.

Table 2. Pressure-Normalized Fluxes of PFOA and PFOMA at Ambient Temperature, 446 kPa Feed Pressure, and 101 kPa Permeate Pressure

		pressure-normalized flux (GPU)[a]						
	FFV[b]	N_2	O_2	H_2	CH_4	C_2H_6	C_3H_8[c]	CO_2
PFOA	0.24	32	74	177	34	40	57	310
PFOMA	0.13	7	18	41	7	6	6	63

[a] 1 GPU = 10^{-6} cm^3 (STP)/(cm^2·s·cmHg). [b] Estimated by a group contribution method.[34] [c] C_3H_8 data were collected at a feed pressure of 308 kPa and a permeate pressure of 101 kPa.

Permeation Properties of PFOA and PFOMA. A representative SEM image of the cross section of a thin-film composite membrane is shown in Figure 2. The lower region corresponds to the microporous PSF support, while the upper region is a PFOMA film with an apparent thickness of 2.1 μm. Pure-gas pressure-normalized fluxes for PFOA and PFOMA at ambient temperature (23 °C) are recorded in Table 2. The estimated uncertainty in these values is less than 10% based on a propagation of error analysis. Permeability coefficients have been determined from the data in Table 2 by assuming that the effective separating layer thickness of each membrane was equal to the separating layer thickness estimated by SEM analysis and are provided in Table 3. Partial penetration of the polymeric separating layer into the microporous substructure of the composite membrane support could affect the magnitude of the effective separating layer thickness; however, we did not observe significant penetration into the membrane support by SEM. Additionally, it was impossible to prepare free-standing films of PFOA or sufficiently large films of PFOMA for permeation testing. The estimated experimental error for all permeability coefficients is less than 20% based on a propagation of error analysis.[32]

Gas permeability coefficients are lower and ideal gas selectivities are higher in PFOMA than in PFOA. Free volume is an important factor influencing diffusion and, consequently, permeation.[33] Based on Bondi's group contribution method, estimated fractional free volume (FFV) values for PFOA and PFOMA are 0.24 and 0.13, respectively.[34] The lower gas permeability coefficients in PFOMA relative to PFOA are consistent with the lower FFV and more restricted chain mobility of PFOMA. Table 3 also shows that permeability values for PFOA and PFOMA seemingly lie between those of TFE/BDD87 and PTFE. Due in part to its high FFV (0.33 based on a density of 1.74 g/cm^3),[35] TFE/BDD87 is the most permeable fluoropolymer known. In contrast, PTFE is highly crystalline, and the estimated FFV for a hypothetical, fully amorphous sample is 0.23.[34,36] Although the estimated FFVs of PFOA and PTFE are comparable, PFOA permeability coefficients are larger than those of PTFE. This trend may reflect two main differences in physical properties. PFOA is amorphous, whereas PTFE is semicrystalline, and crystalline regions in polymers typically act as impermeable barriers to gas transport.[37] Additionally, the long-range segmental motion of PFOA chains is expected to be greater than PTFE because its T_g is more than 100 °C lower than that of PTFE (115–140 °C).[38]

Figure 3 presents the dependence of permeability on penetrant critical volume, a convenient measure of penetrant size. Permeability coefficients for light gases in PFOMA and PFOA decrease in the same order:

$$CO_2 > H_2 > O_2 > N_2 \approx CH_4$$

For rubbery PFOA, hydrocarbon permeability coefficients increase slightly with increasing penetrant size:

$$CH_4 < C_2H_6 < C_3H_8$$

As hydrocarbon number increases, solubility typically increases, which acts to increase permeability, and diffusivity should decrease, which acts to decrease permeability.[33] Many rubbery polymers, such as PFOA and poly(dimethylsiloxane) (PDMS), sieve penetrants weakly on the basis of size,[39] and hence, permeability increases with increasing solubility. In contrast, hydrocarbon permeability coefficients are much lower in PFOMA than in PFOA. In PFOMA, they are nearly independent of hydrocarbon penetrant size, suggesting that PFOMA presents a more strongly size sieving matrix to the penetrants than PFOA, albeit much weaker than that of PS.

Ideal gas selectivities for O_2/N_2 and CO_2/CH_4 are presented in Table 3. For all the fluoropolymers, selectivity decreases as permeability increases. This result is consistent with the well-known tradeoff[40,41] between permeability and selectivity: more permeable polymers are generally less selective and vice versa. Polymers with the best combinations of permeability and selectivity lie on the "upper bound" tradeoff curve. Robeson[40] developed quantitative relations for estimating the upper bound limit of selectivity from experimentally determined permeability coefficients. Table 3 reports the calculated upper bound selectivities. All experimental ideal gas selectivities for PFOA and PFOMA are lower than the calculated upper bound values. The O_2/N_2 selectivity for PFOMA is 48% of the calculated upper bound selectivity. The O_2/N_2 and CO_2/CH_4 selectivities for PFOA are 60% and 50% of the upper bound limits, respectively. These values are closer to the upper bound selectivities than those for other gas pairs studied, i.e., H_2/CH_4, H_2/N_2, and H_2/O_2. In comparison, the ideal pure gas O_2/N_2 selectivities for TFE/BDD87,[35] polysulfone,[42] and PDMS[42] are 77%, 64%, and 62%, respectively, of the calculated upper bound values. These results sug-

Table 3. Gas Permeability Coefficients and Selectivity Values of Selected Fluoropolymers at Ambient Temperature, 446 kPa Feed Pressure, and 101 kPa Permeate Pressure

		permeability coefficient (barrers)[a]							selectivity			
									O_2/N_2		CO_2/CH_4	
	FFV[b]	N_2	O_2	H_2	CH_4	C_2H_6	C_3H_8[c]	CO_2	exptl	calcd[d]	exptl	calcd[d]
TFE/BDD87[e]	0.33	780	1600	3400	600	370	200	3900	2.0	2.6	6.5	8.5
PFOA[f]	0.24	54	130	300	57	68	97	520	2.4	4.0	9.1	18
PFOMA[f]	0.13	15	36	82	14	13	12	130	2.4	5.0	9.1	31
PTFE[g]	0.16	1.3	4.2	9.8	0.74			10	3.2	7.2	13.4	82

[a] 1 barrer = 10^{-10} cm^3(STP)·cm/(cm^2·s·cmHg). [b] Estimated by a group contribution method.[34] [c] C_3H_8 data were collected at a feed pressure of 308 kPa and a permeate pressure of 101 kPa. [d] Calculated from Robeson's correlation:[40] separation factor = $(P_i/k)^{1/n}$ where k = 389 224 and 1 073 700 barrers and n = −5.8000 and − 2.6264 for O_2/N_2 and CO_2/CH_4, respectively. [e] Reference 35. [f] Based on separating layer thicknesses of 1.7 ± 0.3 and 2.0 ± 0.1 μm for PFOA and PFOMA, respectively. [g] This value is the estimated FFV for a hypothetical, fully amorphous sample.[36]

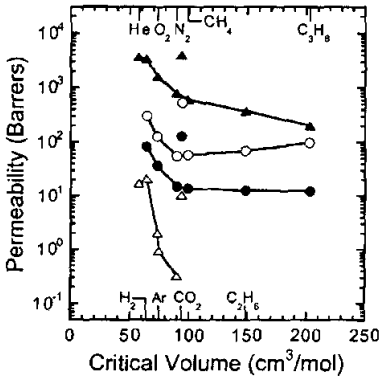

Figure 3. Gas permeability coefficients in PFOA (○), PFOMA (●), PS[50] (△), and TFE/BDD87[35] (▲) at ambient temperature as a function of penetrant critical volume.

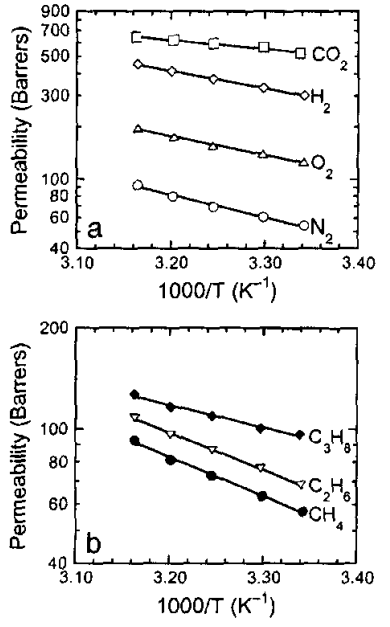

Figure 4. Temperature dependence of gas permeability coefficients for (a) permanent gases and (b) hydrocarbons in PFOA. Shown in (a) are permeability coefficients for N_2 (○), O_2 (△), H_2 (◇), and CO_2 (□). The coefficients for CH_4 (●), C_2H_6 (▽), and C_3H_8 (◆) are displayed in (b). Solid lines correspond to least-squares fits of eq 4 to the data.

gest that PFOMA and PFOA are not attractive materials for industrial gas separations.

Temperature Dependence of Permeability. Figure 4 illustrates the temperature dependence of gas

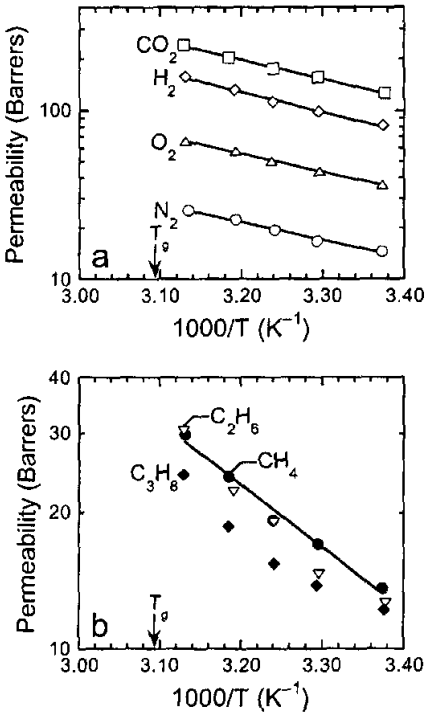

Figure 5. Temperature dependence of gas permeability coefficients for (a) permanent gases and (b) hydrocarbons in PFOMA. Shown in (a) are permeability coefficients for N_2 (○), O_2 (△), H_2 (◇), and CO_2 (□). The coefficients for CH_4 (●), C_2H_6 (▽), and C_3H_8 (◆) are displayed in (b). Solid lines correspond to least-squares regressions of eq 4 to the data (where applicable). The T_g of PFOMA is identified.

permeability in PFOA. The permeability coefficients obey the Arrhenius relation over the temperature range of this study. The temperature dependence of permeability for permanent gases and hydrocarbons in PFOMA is presented in parts a and b of Figure 5, respectively. The Arrhenius plots for the permanent gases in Figure 5a are nearly linear over the entire temperature range tested. However, the corresponding plots for C_2H_6 and C_3H_8 in Figure 5b are not linear. Since the T_g of PFOMA is 50 °C, which is near the upper limit of temperatures explored in this study, this apparent nonlinear behavior is attributed to the permeation measurements of these large penetrants being conducted near T_g. These results are consistent with the diffusion results reported by Kumins and Roteman[43] for a random poly(vinyl chloride-*co*-vinyl acetate) copolymer containing 87% vinyl chloride and 13% vinyl acetate, in which they observed that E_D remained constant for

Table 4. Activation Energies of Gas Permeation (E_P, Expressed in kJ/mol) in PFOA and PFOMA

	N_2	O_2	H_2	CH_4	C_2H_6	C_3H_8	CO_2
PFOA	25 ± 1.2	20 ± 0.7	19 ± 0.2	22 ± 0.8	21 ± 0.5	13 ± 0.9	9.4 ± 0.8
PFOMA	20 ± 1.2	21 ± 0.6	23 ± 1.2	26 ± 1.9	26 ± 3.6[a]	14 ± 1.3[a]	22 ± 0.7
TFE/BDD87[b]	2.2	1.4	1.4	2.3	3.9		0.2

[a] These E_P values are estimates for the glassy state obtained by fitting eq 4 to the permeation data at 23, 30, and 35 °C. [b] Reference 51.

Table 5. Pressure-Normalized Fluxes and Selectivities of PFOA and PS-*b*-PFOA Copolymers at 35 °C, 446 kPa Feed Pressure, and 101 kPa Permeate Pressure

	pressure-normalized flux (GPU)[a]						
	N_2	O_2	H_2	CH_4	C_2H_6	C_3H_8[b]	CO_2
PFOA	41	92	220	43	51	65	350
PS-*b*-PFOA, $\phi_S = 0.12$	19	39	75	18	22	26	140
PS-*b*-PFOA, $\phi_S = 0.24$	12	30	64	14	17	20	110

[a] 1 GPU = 10^{-6} cm^3 (STP)/(cm^2·s·cmHg). [b] C_3H_8 permeability was measured at a feed pressure of 308 kPa and a permeate pressure of 101 kPa.

small penetrants (e.g., He and H_2) but decreased for the largest penetrant investigated (CO_2) below the T_g corresponding to the T_g of poly(vinyl acetate). In the present study, non-Arrhenius behavior is only observed for the largest penetrants investigated (C_2H_6 and C_3H_8), for which the probability of encountering free volume elements of sufficient size to permit diffusion is expected to increase the most upon going from the glassy to the rubbery state.[44] For C_2H_6 and C_3H_8, a rough estimate of E_P in glassy PFOMA was obtained by fitting eq 5 to the permeability data at 23, 30, and 35 °C (i.e., at temperatures below the onset of non-Arrhenius behavior.)

Table 4 presents activation energies of permeation (E_P) for PFOA and PFOMA and, for comparison, TFE/BDD87. These E_P values are estimated from the Arrhenius expression presented previously (eq 5) and are an order of magnitude higher than E_P values for TFE/BDD87. For each gas considered except CO_2, the estimated values of E_P are similar in magnitude for PFOA and PFOMA. The molecular basis for the substantially higher activation energy of permeation of CO_2 in PFOMA is not clear. Activation energies of permeation did not vary systematically with either penetrant critical volume, a convenient measure of penetrant size, or with penetrant critical temperature, a parameter often used to characterize penetrant condensability and consequently solubility.

Permeation Properties of PS-*b*-PFOA Block Copolymers. Pure gas pressure-normalized fluxes for two PS-*b*-PFOA diblock copolymers are provided in Table 5. Permeability coefficients have been calculated from the data in Table 5 using the same method discussed previously and are presented in Table 6. The uncertainty in these values is estimated to be less than 20% based on a propagation of error analysis.[32] In all cases, gas permeability coefficients of PS-*b*-PFOA copolymers lie between those of the PFOA and PS homopolymers. As the PS content of the copolymers increases, gas permeability decreases, while the ideal selectivity increases. The ideal selectivities of the PS-*b*-PFOA copolymers are similar to those of PFOA, suggesting that PFOA constitutes the transport-controlling, continuous microphase. This hypothesis is reasonable since the polymer matrix is composed primarily of PFOA.

Permeation through a structured biphasic material wherein the minor component is randomly dispersed with sharp interfaces in a continuous matrix of the major component is often described by the generalized Maxwell model:[45]

$$P_{struct} = P_c\left[1 + \frac{(1+G)\phi_d}{\left(\frac{P_d/P_c + G}{P_d/P_c - 1}\right) - \phi_d}\right] \qquad (11)$$

where P_{struct} is the permeability of the structured polymer (the PS-*b*-PFOA block copolymer in the present study), and P_c and P_d denote the continuous- and dispersed-phase permeabilities, respectively. The volume fraction of the dispersed phase is given by ϕ_d, and G is a geometric factor accounting for dispersion shape. The upper and lower bounds of the generalized Maxwell model for microphase-separated block copolymers correspond to lamellar morphologies possessing different orientations. If lamellae are oriented parallel to the direction of permeation, $G \to \infty$, and there is minimum resistance to flow. If lamellae are oriented normal to the flow direction, $G \to 0$, and maximum impedance of flow occurs due to obstructive layers of the less permeable component. Estimates of G obtained from the generalized Maxwell model (eq 11) based on the assumption that PFOA is the continuous phase are approximately 10^{-1} for N_2, O_2, CH_4, and CO_2. These results suggest that the morphology of these nanostructured materials is consistent with a highly defective, laminate composite structure in which PS microdomains are oriented perpendicular to the direction of permeation. In this case, the PS-rich regions impede gas flow through the material, resulting in reduced gas permeabilities. However, since these microdomains do not appear to be fully connected, the selectivities are governed by the more permeable PFOA phase. Even if

Table 6. Gas Permeability Coefficients and Selectivities of PFOA, PS, and PS-*b*-PFOA Copolymers at 35 °C, 446 kPa Feed Pressure, and 101 kPa Permeate Pressure

	permeability coefficient (barrers)							selectivity		
	N_2	O_2	H_2	CH_4	C_2H_6	C_3H_8[a]	CO_2	O_2/N_2	H_2/CH_4	CO_2/CH_4
PFOA	70	160	370	73	87	110	590	2.3	5.1	8.1
PS-*b*-PFOA, $\phi_S = 0.12$[c]	23	47	90	22	27	31	170	2.0	4.0	7.7
PS-*b*-PFOA, $\phi_S = 0.24$[d]	19	45	96	21	26	30	170	2.4	4.6	8.1
PS[b]	0.53[52]	2.9[52]	22.6[31]	0.79[52]			12.4[52]	5.5	29	16

[a] C_3H_8 data were collected at a feed pressure of 308 kPa and a permeate pressure of 101 kPa. [b] PS permeability coefficients were determined at 1 atm. [c] Based on estimated separating layer thickness of 1.2 ± 0.2 μm. [d] Based on estimated separating layer thickness of 1.5 ± 0.2 μm.

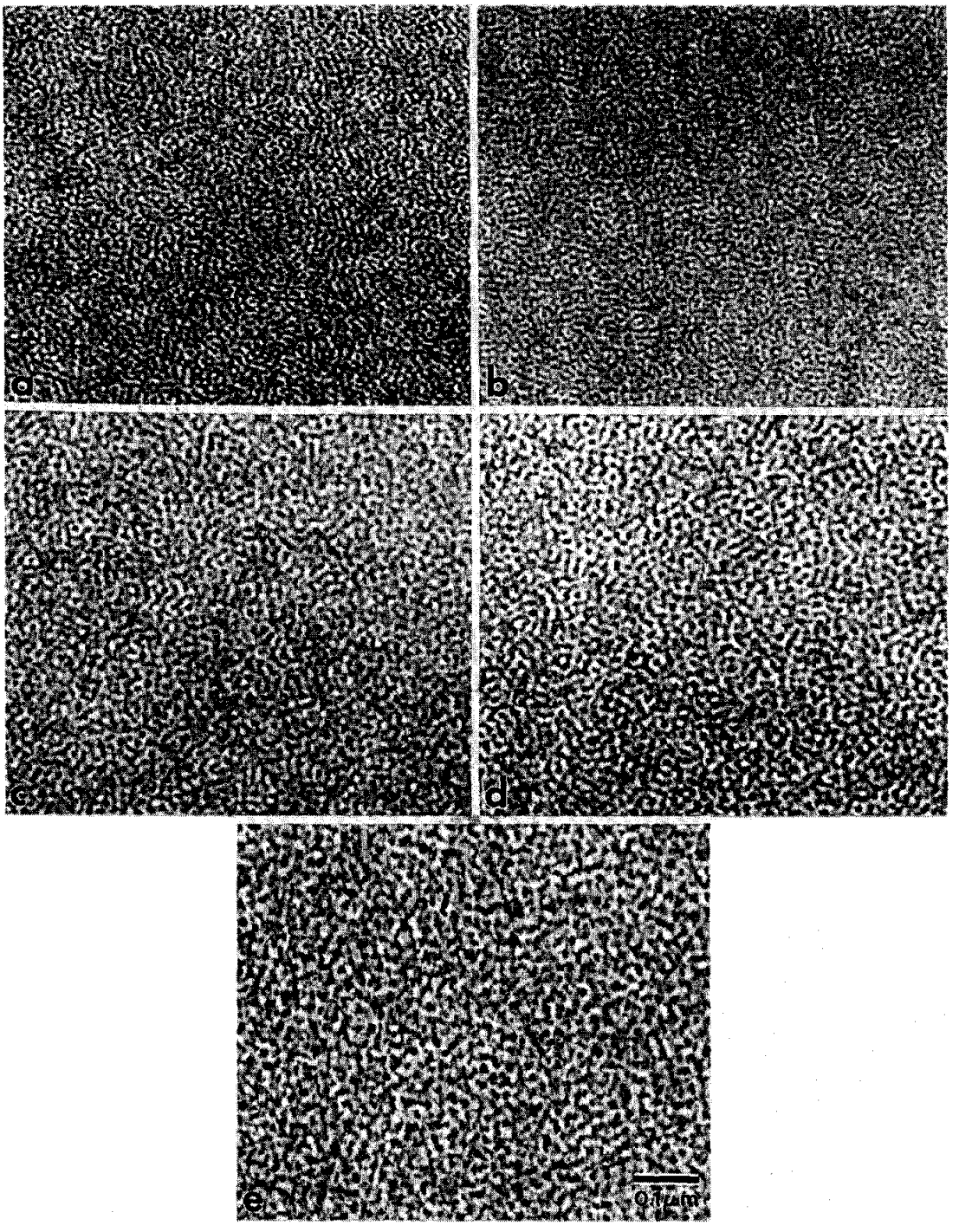

Figure 6. Transmission electron micrographs of PS-*b*-PFOA diblock copolymers in which the PS microdomains appear dark due to selective staining. All the copolymers consist of a PS block with $\bar{M}_n$ = 3700, whereas the $\bar{M}_n$ of the PFOA block is varied as follows: (a) 13 700, (b) 27 500, (c) 39 800, (d) 61 200, and (e) 244 500. The corresponding PS volume fractions (ϕ_S) of these copolymers are (a) 0.31, (b) 0.18, (c) 0.13, (d) 0.09, and (e) 0.02.

the PS domains were fully connected to form a co-continuous structure, PS permeability coefficients are so much lower than those of PFOA that the separation properties of the sample would still be governed by those of PFOA because most of the gas permeation would occur through PFOA-rich regions.

Morphological Characteristics of PS-*b*-PFOA Block Copolymers. Transmission electron micrographs of five PS-*b*-PFOA copolymers composed of PS blocks of constant $\bar{M}_n$ (3700) and PFOA blocks differing in $\bar{M}_n$ (from 13 700 to 244 500) are displayed in Figure 6. In these images, the PS microdomains appear electron-

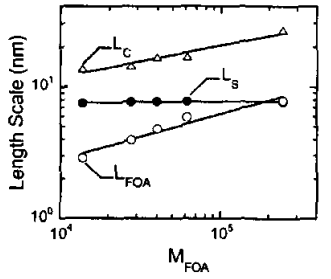

Figure 7. Variation of L_S (●), L_{FOA} (○), and L_c (△) with M_{FOA} on double-logarithmic coordinates for the five PS-*b*-PFOA diblock copolymers displayed in Figure 6. The solid lines are power-law fits to the data, and their slopes yield the values of α reported in the text.

opaque (dark) due to selective RuO_4 staining. The copolymers with PFOA blocks of $\bar{M}_n$ = 27 500 and 39 800, shown in parts b and c of Figure 6, respectively, consist of 18 and 13 vol% PS and are similar in composition to the block copolymers used in the gas permeation studies (ϕ_S = 0.24 and 0.12). Since the morphologies in these micrographs confirm that the copolymers are microphase-separated but do not resemble any of the established (classical or complex) morphologies (despite the slow solvent evaporation procedure employed during preparation), it is reasonable to expect that the copolymers used in the permeation studies possess similar, but possibly more refined, morphologies (due to their higher $\bar{M}_n$) than those in Figure 6b,c. No evidence of long-range order exists in any of these materials, most likely due to their molecular weight *and* (anticipated) compositional polydispersity.[46] At each composition, the PFOA microphase appears continuous. In particular, regions of co-continuous PS and PFOA channels exist in Figure 6b,c, suggesting that these morphologies may exhibit bicontinuity.[47] Such nanostructures are also consistent with the highly defective lamellar morphology previously inferred from the permeation results.

The characteristic dimensions of the morphologies displayed in Figure 6 are presented in Figure 7 and include the average thicknesses of the PS and PFOA microdomains (L_S and L_{FOA}, respectively) acquired from real-space measurements, as well as the average correlation length (L_c) derived from the correlation maxima in 2D Fourier transforms of the images. These dimensions are presented on double-logarithmic coordinates as a function of the PFOA block mass (M_{FOA}) in Figure 7. As expected from the molecular characteristics of these copolymers, L_S remains invariant with respect to M_{FOA}, since the PS block mass (M_S) does not vary in the copolymer series. In contrast, L_{FOA} is seen to increase with increasing M_{FOA}. It immediately follows (and is observed) that L_c likewise increases with an increase in M_{FOA}. The relationships evident in Figure 7 therefore correctly reflect the variation in molecular characteristics of the copolymers investigated in this work. Closer examination of the dependence of these dimensions on molecular weight may provide insight into the extent of molecular anisotropy.

Block copolymers exhibit three ordered regimes determined by the degree of block segregation: strong, intermediate, and weak. A convenient measure of these segregation regimes is the thermodynamic incompatibility, designated χN, where χ denotes the Flory–Huggins interaction parameter and N is the number of statistical units along the copolymer backbone. Within these regimes, the blocks stretch to different extents, and the extent of block stretching governs the characteristic dimensions of the microphase-separated morphologies. The data in Figure 7 reveal that both L_{FOA} and L_c increase as M_{FOA}^{α}, where α is equal to 0.34 ± 0.01 for L_{FOA} and 0.24 ± 0.01 for L_c. In contrast, L_S remains relatively constant at about 7.7 nm. Since the gyration diameter (D_g) of unperturbed PS with $\bar{M}_n$ = 3700 is estimated to be ca. 3.4 nm,[48] the PS microdomains correspond to about $2.2D_g$ in thickness, indicating that the PS blocks are slightly stretched along the interfacial normal.

Since α provides a measure of the degree of block stretching, it could, in principle, be used to assign copolymers to one of the segregation regimes listed above. According to recent theoretical considerations,[49] values of α for ordered monomolecular copolymers are predicted to be about 0.67 in the strong-segregation regime, 0.80 in the intermediate-segregation regime, and 0.99 in the weak-segregation regime. The values of α derived from L_{FOA} and L_c in Figure 7 for the PS-*b*-PFOA copolymers do not match, however, any of these predicted scaling exponents. This disagreement may be due to copolymer material considerations (e.g., molecular or compositional polydispersity), in which chain packing and interfacial curvature vary due to local differences in block length. Another, more likely explanation for the apparent disagreement with theory is attributed to overlap of projected PS microdomains in the TEM images. Since the PS microdomains are significantly smaller (ca. 7.7 nm) than a typical TEM section (ca. 100 nm), each TEM image constitutes a projection through several microdomain layers. The resultant superimposed image complicates conventional analysis of α. Thus, we conclude that the values of α measured here cannot be used to discern the segregation regime in which these PS-*b*-PFOA copolymers reside. Because of uncertainties in the value of χ between PS and PFOA and the impact of molecular weight/compositional polydispersity on χ, no attempt is likewise made to estimate the magnitude of χN for these copolymers.

Reexamination of the DSC data provided in Table 1, coupled with the T_g calculations provided earlier in this work, reveals that the T_g's of some of the PS blocks are depressed below what is expected on the basis of molecular weight. In contrast, the T_g's of the PFOA blocks differ only slightly from that of the PFOA homopolymer. These two observations taken together suggest that the PS microdomains are not completely demixed. While it remains uncertain at this time whether such residual mixing is attributed to thermodynamic or kinetic considerations (or a combination thereof), the existence of residual mixing in a microphase-separated block copolymer strongly suggests that χN is depressed relative to a highly demixed copolymer in the strong-segregation regime.

Conclusions

The temperature-dependent permeation properties of PFOA, PFOMA, and PS-*b*-PFOA diblock copolymers are reported for a family of gases. In general, PFOMA possesses lower gas permeabilities and higher selectivities than PFOA, which is consistent with its lower fractional free volume and, based on T_g, more restricted chain mobility. The activation energy of permeation for PFOMA increases for larger penetrants (e.g., C_2H_6 and

C_3H_8) as T_g is approached from below. For small penetrants, such as N_2 and O_2, no change in E_P is observed near T_g. The permeation and morphological characteristics of PS-*b*-PFOA diblock copolymers have also been investigated. The PS-*b*-PFOA copolymers exhibit microphase-separated morphologies with no evidence of long-range order, which is attributed to the molecular weight/compositional polydispersity of the copolymer molecules. These copolymers possess gas permeabilities intermediate between those of rubbery, highly permeable PFOA and glassy, relatively impermeable PS, and the permeability coefficients decrease with increasing PS content. The gas permeabilities and selectivities suggest that the morphologies are highly defective laminate structures and are consistent with results from electron microscopy.

Acknowledgment. This work was supported in part by the Office of Naval Research, the National Science Foundation (Presidential Faculty Fellowship: J. M. D. 1993−1997), and the STC program of the National Science Foundation under Agreement No. CHE9876674. We thank M. Gregory of the NCSU Analytical Instrumentation Facility for technical assistance.

References and Notes

(1) DeSimone, J. M.; Guan, Z.; Elsbernd, C. S. *Science* **1992**, *257*, 945.
(2) Emissions of greenhouse gases in the United States, Energy Information Administration, DOE/EIA-0573(96), Washington, DC, Oct 1997.
(3) Wall, L. A. *Fluoropolymers*; John Wiley & Sons: New York, 1972.
(4) Guan, Z.; Elsbernd, C. S.; DeSimone, J. M. *Polym. Prepr. (Am. Chem. Soc., Div. Polym. Chem.)* **1992**, *33*, 329.
(5) Guan, Z.; DeSimone, J. M. *Macromolecules* **1994**, *27*, 5527.
(6) Spontak, R. J.; Alexandridis, P. *Curr. Opin. Colloid Interface Sci.* **1999**, *4*, 140.
(7) Bates, F. S.; Fredrickson, G. H. *Phys. Today* **1999**, *52*, 32.
(8) Bondar, V. I.; Freeman, B. D.; Pinnau, I. *J. Polym. Sci., Part B: Polym. Phys.* **1999**, *37*, 2463.
(9) Csernica, J.; Baddour, R. F.; Cohen, R. E. *Macromolecules* **1989**, *22*, 1493.
(10) Csernica, J.; Baddour, R. F.; Cohen, R. E. *Macromolecules* **1990**, *23*, 1429.
(11) Rein, D. H.; Csernica, J.; Baddour, R. F.; Cohen, R. E. *Macromolecules* **1990**, *23*, 4456.
(12) Rein, D. H.; Baddour, R. F.; Cohen, R. E. *J. Appl. Polym. Sci.* **1992**, *45*, 1223.
(13) Sax, J. E.; Ottino, J. M. *Polymer* **1985**, *26*, 1073.
(14) Shah, N.; Sax, J. E.; Ottino, J. M. *Polymer* **1985**, *26*, 1239.
(15) Koshimura, K.; Sato, H. *Polym. Bull.* **1992**, *29*, 705.
(16) Odani, H.; Taira, K.; Nemoto, N.; Kurata, M. *Bull. Inst. Chem. Res.* **1975**, *53*, 216.
(17) Sukhanova, T. Y.; Kuznetsov, Y. P.; Kruchinina, Y. V.; Lukashova, N. V.; Sidorovich, A. V.; Gusinskaya, V. A.; Peltsbauer, Z. *Polym. Sci. U.S.S.R. (Engl. Transl.)* **1989**, *31*, 2741.
(18) Tsujita, Y.; Yoshimura, K.; Yoshimizu, H.; Takizawa, A.; Kinoshita, T.; Furukawa, M.; Yamada, Y.; Wada, K. *Polymer* **1993**, *34*, 2597.
(19) Ghosal, K.; Freeman, B. *Polym. Adv. Technol.* **1994**, *5*, 673.
(20) Graham, T. *London Edinburgh Dublin Philos. Mag. J. Sci.* **1866**, *32*, 401.
(21) Meares, P. *J. Am. Chem. Soc.* **1954**, *76*, 3415.
(22) Otsu, T.; Kuriyama, A. *Polym. Bull.* **1984**, *11*, 135.
(23) Otsu, T.; Kuriyama, A. *Polym. J.* **1985**, *17*, 97.
(24) Betts, D. E. Ph.D. Dissertation, The University of North Carolina at Chapel Hill, 1998.
(25) Crank, J.; Park, G. S. In *Diffusion in Polymers*; Crank, J., Park, G. S., Eds.; Academic: New York, 1968; p 452.
(26) Stern, S. A.; Gareis, P. J.; Sinclair, T. F.; Mohr, P. H. *J. Appl. Polym. Sci.* **1963**, *7*, 2035.
(27) Utracki, L. A. *Polymer Alloys and Blends*; Hanser: Berlin, 1990.
(28) Kane, L.; Satkowski, M. M.; Smith, S. D.; Spontak, R. J. *J. Polym. Sci., Polym. Phys. Ed.* **1997**, *35*, 2653.
(29) Lu, X.; Jiang, B. *Polymer* **1991**, *32*, 471.
(30) Resnick, P. R.; Buck, W. H. In *Modern Fluoropolymers*; Scheirs, J., Ed.; John Wiley & Sons: New York, 1997; p 397.
(31) Pauly, S. In *Polymer Handbook*; Brandrup, J., Immergut, E., Eds.; John Wiley and Sons: New York, 1989; p VI/435.
(32) Bevington, P. R.; Robinson, D. K. *Data Reduction and Error Analysis for the Physical Sciences*, 2nd ed.; McGraw-Hill: New York, 1992.
(33) Freeman, B. D.; Pinnau, I. In *Polymer Membranes for Gas and Vapor Separations: Chemistry and Materials Science*; Freeman, B. D., Pinnau, I., Eds.; ACS Symp. Ser.; American Chemical Society: Washington, DC, 1999; Vol. 733, p 1.
(34) Bondi, A. *J. Phys. Chem.* **1964**, *68*, 441.
(35) Pinnau, I.; Toy, L. G. *J. Membr. Sci.* **1996**, *109*, 125.
(36) Van Krevelen, D. W. *Properties of Polymers*, 3rd ed.; Elsevier Science: Amsterdam, The Netherlands, 1990.
(37) Vieth, W. R. *Diffusion In and Through Polymers*; Hanser: New York, 1991.
(38) Koo, G. P. In *Fluoropolymers*; Wall, L. A., Ed.; John Wiley & Sons: New York, 1972; Vol. XXV, p 507.
(39) Koros, W. J.; Hellums, M. W. In *Encyclopedia of Polymer Science and Engineering*; Kroschwitz, J. I., Ed.; John Wiley & Sons: New York, 1990; p 1211.
(40) Robeson, L. M. *J. Membr. Sci.* **1991**, *62*, 165.
(41) Freeman, B. D. *Macromolecules* **1998**, *32*, 375.
(42) Baker, R. W. *Membrane Technology and Applications*; McGraw-Hill: New York, 2000.
(43) Kumins, C. A.; Roteman, J. *J. Polym. Sci.* **1961**, *55*, 683.
(44) Stannett, V. In *Diffusion in Polymers*; Crank, J., Park, G. S., Eds.; Academic: New York, 1968; p 41.
(45) Petropoulos, J. H. *J. Polym. Phys., Polym. Phys. Ed.* **1985**, *23*, 1309.
(46) Burger, C.; Ruland, W.; Semenov, A. N. *Macromolecules* **1990**, *23*, 3339.
(47) Hashimoto, T.; Koizumi, S.; Hasegawa, H.; Isumitani, T.; Hyde, S. T. *Macromolecules* **1992**, *25*, 1433.
(48) Jinnai, H.; Nishikawa, Y.; Spontak, R. J.; Smith, S. D.; Agard, D. A.; Hashimoto, T. *Phys. Rev. Lett.* **2000**, *84*, 518.
(49) Matsen, M. W.; Bates, F. S. *Macromolecules* **1996**, *29*, 1091.
(50) Rudd, J. F. In *Polymer Handbook*, 3rd ed.; Brandrup, J., Immergut, E. H., Eds.; John Wiley & Sons: New York, 1989; p V/81.
(51) Merkel, T. C.; Bondar, V.; Nagai, K.; Freeman, B. D.; Yampolskii, Y. P. *Macromolecules* **1999**, *32*, 8247.
(52) Puleo, A. C.; Murganandam, N.; Paul, D. R. *J. Polym. Sci., Polym. Phys. Ed.* **1989**, *27*, 2385.

MA010355I